Earth and Space Science

RESEARCH ARTICLE
10.1029/2023EA002991

Estimating Three-Dimensional Structures of Eddy in the South Indian Ocean From the Satellite Observations Based on the isQG Method

Zhiqiang Chen[1,2], Xidong Wang[1,3], Lei Liu[4], and Xiaoting Wang[5]

[1]College of Oceanography, Hohai University, Nanjing, China, [2]GEOMAR Helmholtz Centre for Ocean Research Kiel, Kiel, Germany, [3]Laboratory for Regional Oceanography and Numerical Modeling, Qingdao National Laboratory for Marine Science and Technology, Qingdao, China, [4]State Key Laboratory of Tropical Oceanography, South China Sea Institute of Oceanology, Chinese Academy of Sciences, Guangzhou, China, [5]Beijing Aviation Meteorological Institute, Beijing, China

Key Points:

- The high-resolution eddy's 3D structures are estimated from the satellite observations based on the interior + surface quasigeostrophic (isQG) method
- Introducing the higher-resolution sea surface temperature observation to isQG method enhances the effective resolution of reconstruction
- A correction scheme in density reconstruction within the mixed layer is suggested to offset the absence of mixed layer dynamics

Supporting Information:

Supporting Information may be found in the online version of this article.

Correspondence to:

X. Wang,
xidong_wang@hhu.edu.cn

Citation:

Chen, Z., Wang, X., Liu, L., & Wang, X. (2023). Estimating three-dimensional structures of eddy in the South Indian Ocean from the satellite observations based on the isQG method. *Earth and Space Science*, *10*, e2023EA002991. https://doi.org/10.1029/2023EA002991

Received 19 APR 2023
Accepted 23 SEP 2023

Author Contributions:

Formal analysis: Zhiqiang Chen
Methodology: Zhiqiang Chen
Project Administration: Xidong Wang
Supervision: Xidong Wang
Writing – original draft: Zhiqiang Chen
Writing – review & editing: Xidong Wang, Lei Liu, Xiaoting Wang

Abstract By incorporating the high-resolution satellite remote sensing sea surface temperature (SST) with low-resolution sea level anomaly and sea surface salinity (SSS), this study explores the reconstructability of the three-dimensional (3D) eddy structures via the "interior + surface quasigeostrophic" (isQG) method in the South Indian Ocean. We apply the incorporation of high-resolution SST to improve the spatial resolution of the reconstruction. We also propose a correction scheme for density reconstruction within the mixed layer to offset the absence of mixed layer dynamics in the SQG framework. Comparison against the in situ observations demonstrates a satisfactory reconstructability for subsurface velocity and density anomalies. Statistically, the zonal velocity reconstructability outperforms its meridional counterpart and the corresponding velocity phase. The reconstructed shallow-layer velocity exhibits a superior skill in eddy-active regions, when compared with drogued drifter observations. Reconstructed subsurface velocities reproduce the spatial structures of eddy-induced velocity anomaly along the GO-SHIP observation transect, although present smaller magnitudes. Results demonstrate the potential applicability of the isQG method for reconstructing mesoscale eddies, particularly in the ocean at mid-to-high latitudes, where subsurface dynamics are strongly influenced by barotropic and the first baroclinic modes. With the upcoming high-advanced satellite observations, the isQG framework is expected to achieve better subsurface estimations.

Plain Language Summary The South Indian Ocean (SIO) contains a significant number of mesoscale eddies that have been thoroughly studied for their horizontal structure, lifetime, and trajectory through satellite observations, particularly using the gridded sea level anomaly maps. Although the contributions of eddies to oceanic energy balance and material transports have become increasingly clear, understanding the three-dimensional (3D) structures of smaller-scale eddies in the SIO remains a challenge due to insufficient subsurface observations and the relatively low effective resolution of current satellite-gridded sea surface height (SSH) products. This study investigates the potential of dynamically reconstructing the subsurface 3D structures of SIO eddies from satellite observations. We combine higher-resolution sea surface temperature snapshots with the SSH map to enhance the effective resolution of the reconstructed subsurface density and velocity anomalies, which enables the reproduction of smaller-scale structures associated with temperature fronts. We also propose a correction scheme to increase the reconstructability of the density anomaly within the mixed layer. Evaluations against multisource real observations suggest a satisfactory reconstructability of the interior + surface quasigeostrophic method for the eddy's 3D structures. This study would provide a new way to investigate the 3D structures of eddy's evolution.

1. Introduction

Oceanic mesoscale eddies with horizontal scales of 50–300 km, which are vital transporters of marine materials (Chelton, Gaube, et al., 2011; C. Dong et al., 2014; McGillicuddy et al., 2007; Y. Zhang et al., 2014; Z. Zhang et al., 2014), have been ubiquitously observed in the world oceans since the 1960s (Chelton, Schlax, et al., 2011). Eddies are widely spread in the South Indian Ocean (SIO) because of its unique circulation system (as shown in Figure 1) and profoundly affect the local energy transfer and material transport (Buongiorno Nardelli et al., 2018; Nencioli et al., 2018; Sheen et al., 2014; Zheng et al., 2015). For instance, the Agulhas Current transports high-temperature/salinity water from the SIO to the Atlantic Ocean in the form of Agulhas leakage (e.g., Beal

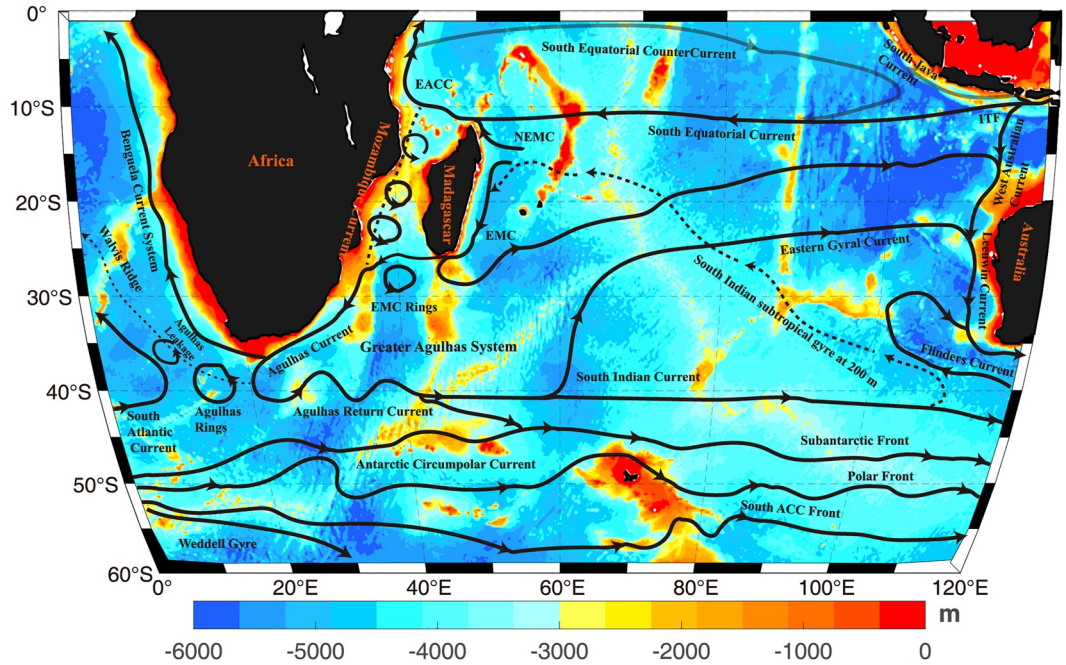

Figure 1. South Indian Ocean schematic surface circulation (arrow shaped) and bottom topography (shading). Black arrows: mean flows without seasonal reversals. Gray arrows: monsoonal reversing circulation. Black dotted arrows: the subsurface current. Acronyms: EACC, East African Coastal Current; ITF, Indonesian Throughflow; NEMC, Northeast Madagascar Current; EMC, East Madagascar Current (adopted from Beal et al., 2011; Talley et al., 2011).

& Bryden, 1997; Casanova-Masjoan et al., 2017; Souza et al., 2011), thus impacting the Atlantic circulation on a variety of spatiotemporal scales (Beal et al., 2011; Biastoch, Böning, et al., 2008; Biastoch, Lutjeharms, et al., 2008; Biastoch et al., 2015; Capuano et al., 2018). The eddies also lead to trans-latitude heat and salt redistribution, affecting marine organisms' reproduction and migration in SIO (e.g., Dufois et al., 2017; Gaube et al., 2013; José et al., 2014; X. Wang et al., 2012). Extensive and in-depth investigations have been conducted on the horizontal structure, lifetime, and trajectory of eddies based on multisource data to determine their influence on other dynamical processes (Arbic et al., 2013; Chelton, Schlax, et al., 2011; G. Chen et al., 2011; C. Dong et al., 2022; Stammer, 1998; G. Yang et al., 2013; Zhai et al., 2010). A few studies have examined the feasibility of compositing the three-dimensional (3D) mean structure of the eddies based on satellite altimeter and in situ data, taking into account the eddy-associated vertical exchanges (Chaigneau et al., 2011; Ferrari & Wunsch, 2009; Pegliasco et al., 2015; Qiu & Chen, 2005; Z. Zhang et al., 2014).

Understanding the 3D structures of eddies is crucial for accurately quantifying their contribution to the eddy-associated exchanges, but our knowledge of their specific 3D structure, generation, and dissipation remains fragmentary due to the lack of systematic subsurface measurements (Hughes & Wilson, 2008; Sen et al., 2008; Z. Zhang et al., 2016). Despite the increase of in situ observations over the past two decades (Brett et al., 2020; Z. He et al., 2021; Riser et al., 2016), historical data can only support an understanding of the general 3D structure of eddies (D. Dong et al., 2017; Y. He et al., 2021; Z. Zhang et al., 2014); it is a challenge to fully capture evolving oceanic eddies in terms of their specific 3D structures from in situ observations. Previous studies have used composite analyses (Y. He et al., 2021; Nencioli et al., 2018; Y. Yang et al., 2019; Z. Zhang et al., 2014) or the analytical solution of the eddy's mean structure (Z. Zhang, Zhang, et al., 2013), along with sea level anomaly (SLA) and in situ observations, to composite the 3D structure of the eddy. In places like the Kuroshio and South China Sea, where in situ observations are occasionally sufficient, such composite approaches have been successfully implemented (Qiu & Chen, 2005; G. Yang et al., 2013; Y. Yang et al., 2019; Z. Zhang, Zhao, et al., 2013). However, such composite approaches have limited application in the SIO due to insufficient in situ observations that cannot identify the 3D structure of smaller mesoscale eddies and their evolution process. Other methods are eagerly required to adequately reproduce the eddy's 3D structure in the SIO, where the first baroclinic Rossby radius of deformation is about 5–50 km at mid-to-high latitudes (Chelton et al., 1998; LaCasce & Groeskamp, 2020).

The surface quasigeostrophic (SQG) theory provides a reasonable framework to use well-sampled surface information to reconstruct oceanic subsurface 3D structures (Klein & Lapeyre, 2009; Lapeyre, 2017). It can depict the upper ocean dynamics for scales between 10 and 400 km (Isern-Fontanet et al., 2008; Lapeyre & Klein, 2006). Over the past two decades, the SQG theory has been extensively explored within the oceanographic context (e.g., Chavanne & Klein, 2016; Z. Chen et al., 2020; González-Haro & Isern-Fontanet, 2014; Isern-Fontanet et al., 2006, 2014; Klein et al., 2009; LaCasce, 2012; LaCasce & Mahadevan, 2006; LaCasce & Wang, 2015; L. Liu et al., 2014, 2017; Miracca-Lage et al., 2022; Ponte & Klein, 2013; Ponte et al., 2013; Yan et al., 2020, 2021). Two reconstruction methods are developed based on the SQG theory: the "effective" SQG (eSQG) and the "interior plus surface QG" (isQG) methods. The eSQG method was first put forward by Lapeyre and Klein (2006) and then developed by Isern-Fontanet et al. (2008, 2014). It can only require a single snapshot of sea surface temperature (SST), sea surface salinity (SSS), or sea surface density anomaly (SSDA) to obtain subsurface velocities (Isern-Fontanet et al., 2017). Although the eSQG method has been fruitfully investigated (González-Haro et al., 2020; Isern-Fontanet et al., 2008, 2014; Qiu et al., 2016, 2020), its practical application is limited by the idealized assumptions of good correlation between sea surface density (SSD) and sea surface height (SSH; Lapeyre & Klein, 2006). J. Wang et al. (2013) proposed a more elaborate isQG method, which employs SSH and SSD to constrain the surface and subsurface potential vorticity (PV) simultaneously and is insensitive to the SSD–SSH phase shift. The satisfactory isQG reconstructability has been demonstrated in the context of ocean model outputs and in the real oceans (L. Liu & Xue, 2022; L. Liu et al., 2017, 2019, 2021; Yan et al., 2020, 2021). L. Liu et al. (2014) and Z. Chen et al. (2020) indicated that the isQG method is promising for reconstructing the 3D structure of oceanic mesoscale eddies from ocean surface information in the SIO.

The effective resolution of the current satellite-gridded SSH products is ∼150–200 km in space and ∼30 days in time in the SIO (Ballarotta et al., 2019; Pujol et al., 2012; Taburet et al., 2019). When applied in the real oceans, the isQG method is inevitably restricted by the current resolution of SSH: the eddy's 3D structures could not be properly reconstructed, especially when the eddy gets smaller. By incorporating the higher-resolution satellite SST-gridded product (Gentemann, 2003; M. Martin et al., 2012; Reynolds & Chelton, 2010; Rio & Santoleri, 2018) with the current lower-resolution satellite SSH, the first objective of our work is to enhance the effective resolution of isQG subsurface reconstructions. The other two objectives are to (a) improve the density anomaly reconstruction in the mixed layer, which is marginally captured by the isQG method and (b) evaluate the reconstructed high-resolution velocity and density fields using multisource in situ observations. The rest of this study is structured as follows. Section 2 provides an overview of the data, followed by an introduction of the method in Section 3. The reconstruction and evaluation of the isQG-reconstructed subsurface 3D structures are described in Section 4. The conclusion and discussion are given in Section 5.

2. Data

2.1. Satellite-Gridded Data

Three kinds of satellite observations are used in this study, including SLA, SST, and SSS. The daily, 1/4° map of SLA is from the Copernicus Marine Environment Monitoring Service Sea Level Thematic Assembly Center (CMEMS-TAC) and estimated using optimal interpolation of data from all available altimeter missions with respect to the mean dynamic topography (MDT) over 1993–2012 (Mulet et al., 2021). The daily gridded SST product is obtained from Remote Sensing Systems (2023), which combines the through-cloud capabilities of microwave data and high spatial resolution of infrared SST data to produce the MWIRSST product. Version 5 of this product is calculated using optimal interpolation with 100 km and 4-day correlation scales on a 0.09° regular grid (M. Martin et al., 2012; Reynolds & Chelton, 2010; Rio & Santoleri, 2018). It is worth noting that the presence of high-variability clouds can hamper the quality of infrared observations, thereby causing the effective resolution of SST to deviate from its grid spacing (Reynolds et al., 2013). The daily, 1/20° map of the SMOS-Barcelona Expert Center (BEC) SSS data set, covering January 2011 to May 2021, is processed by the BEC and generated following a debiased non-Bayesian approach presented in Olmedo et al. (2017). The SMOS-BEC SSS data set is fused by the multifractal fusion algorithm with the template of OSTIA SST (Olmedo et al., 2021). This improves the resolution and mitigates the noises of SSS but could ruin some temperature-independent salinity signals simultaneously (Buongiorno Nardelli, 2012), decreasing the effective resolution of this product.

We also employ two types of satellite-derived velocity fields. The first is the surface geostrophic currents derived from the standard Data Unification and Altimeter Combination System (DUACS) SSH maps (Taburet

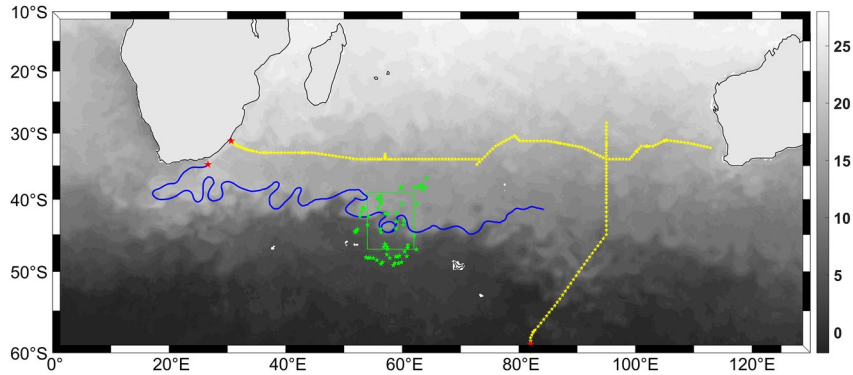

Figure 2. Location schematic of the observations introduced in Section 2. Red five-pointed stars are the starting positions of in situ observations. Yellow five-pointed stars are the observation stations of the cruises 2009-I05-US (west-east direction) and 2016-I08S-US (south-north direction), respectively. Green five-pointed stars are the locations of an eddy-trapped Argo float from 15 June to 30 August 2015. The blue line is the trajectory of drifter 127198 from 13 April to 27 September 2015. Green box is the edge of the case study shown in Section 4.1. Shading is the sea surface temperature (SST) snapshot on 17 July 2015.

et al., 2019). The second is the climatology geostrophic current, serving as the surface background current, which is obtained from the 1/8° gridded MDT and distributed by the CMEMS-TAC (Mulet et al., 2021).

2.2. In Situ Data

The isQG method requires the squared buoyancy frequency (N^2) profile as input. Here, the monthly gridded temperature and salinity (T/S) fields from the In Situ Analysis System (ISAS) are employed to derive the region-averaged N^2 profile from 0 to 1,500 m. The temperature and salinity fields produced in the latest version of ISAS20-ARGO preserve as much as possible the time and space sampling capabilities of the Argo network of profiling floats between 2002 and 2020, with 187 standard depths between 0 and 5,500 m and 0.5° × 0.5° global horizontal grid (Gaillard et al., 2016; Kolodziejczyk et al., 2021).

Three sorts of in situ observations are employed to evaluate the isQG-reconstructed geostrophic velocity and density fields. Using satellite-tracked drifters, the Global Drifter Program (GDP) has been observing the ocean current at 15 m depth for over 20 years. It becomes a reliable way to monitor the oceanic near-surface current system (Laurindo et al., 2017; Lumpkin et al., 2013). A drifter numbered 127198 is chosen within its drogued life as a testbed. T/S profiles from GO-SHIP provided by CLIVAR and the Carbon Hydrographic Data Office are used. The program supports oceanographic research by providing access to high-quality, global, vessel-based conductivity temperature depth and hydrographic data from GO-SHIP, WOCE, CLIVAR, and other repeat hydrography programs. T/S profiles from cruises 2009-I05-US (ExpoCode: 33RR20090320) and 2016-I08S-US (ExpoCode: 33RR20160208) are specifically chosen. A z-direction low-pass filter (five grids smooth) is applied to the original T/S observations to exclude the influence of vertical high-frequency signals. The WOA18 monthly climatology T/S data sets are also employed as the background thermohaline fields. They are the objectively interpolated mean fields for oceanographic variables at standard depth levels for the world ocean, with 1/4° spatial resolution and a depth range of 0–1,500 m.

All the T/S fields above are used to calculate the potential density via the TEOS-10 equation (IOC et al., 2010). Figure 2 depicts the location schematic of these observations.

2.3. Reanalysis Data

The currents from GLORYS12V1 are employed to validate the reconstructed currents independently. The GLORYS12V1 is a global eddy-resolving physical ocean and sea ice reanalysis at 1/12° horizontal resolution covering the altimetry (1993 onward), designed and implemented in the framework of the CMEMS (Jean-Michel et al., 2021).

2.4. Data Preprocessing

The isQG method requires SSH anomaly (SSHA), SSDA, and the N^2 profile as inputs. To address the issue of inconsistent spatial resolution between satellite SST and SLA, we linearly interpolate the low-resolution SLA

map in each reconstruction area to match the resolution of SST and then apply a low-pass filter to eliminate interpolation-induced noise. This processed field is defined as the input SSHA field. The filter's cut-off wavelength (L_c) is determined by the kinetic energy (KE) spectra derived from surface velocities calculated by the SLA and SSDA based on geostrophic approximation and the eSQG method, respectively. More details are available in Figure S1 in Supporting Information S1, and the details of the eSQG method are shown in Appendix A. The spatial filter employs spectral truncation to extract the target scales, which performs a Fourier low-pass filter at a given cut-off wavelength. Readers may refer to Sections 2 and 4 of Zhou and Cheng (2021) for details.

To obtain SSDA, we first interpolate the SMOS-BEC SSS and the WOA18 monthly climatology T/S fields to the same grid as SST. A low-pass filter with 100 km (4 times than the grid resolution) cut-off wavelength acts on the interpolated WOA18 monthly climatology fields to exclude the noise generated by interpolation. Then, the interpolated SMOS SSS and the input SST fields are used to generate the daily SSD. The preprocessed monthly climatology T/S fields are combined to derive the background SSD field. Finally, the SSDA is the difference between the daily and background SSD fields. Besides, we use the monthly climatology salinity field to calculate the daily SSD before 24 January 2011.

The squared buoyancy frequency is calculated as $N^2 = -g/\rho_v(\partial\rho/\partial z)$, where g is the gravity constant. ρ_v and ρ are the reference density and potential density, respectively.

3. Method

3.1. Reconstruction Method and Experiment Setup

The isQG method proposed by J. Wang et al. (2013) has been fruitfully utilized to reconstruct subsurface density and geostrophic velocity fields from sea surface observations and a stratification profile (Z. Chen et al., 2020; L. Liu & Xue, 2022; L. Liu et al., 2014, 2017; Miracca-Lage et al., 2022; Yan et al., 2020, 2021). As an extension of the SQG framework, the isQG method recognizes that the oceanic PV can be decoupled into an SQG (surface) component and an interior component, with the former associated with SSDA and the latter dominated by stratification. Details of the isQG method are given in Appendix A. The N^2 profile derived from in situ observations could not be directly used by the isQG method. Typically, the N^2 value approaching zero near the surface can result in unrealistic overshoots in the mixed layer when solving the SQG component. To resolve this issue, most previous studies idealized the mixed layer N^2 as follows: (a) replacing the surface value with a mixed layer averaged one and (b) linearly interpolating the N^2 in the mixed layer using the substituted surface value and the value at the base of the mixed layer (e.g., L. Liu et al., 2017; J. Wang et al., 2013). Inevitably, this modification could be inadequate when applying the observed N^2 profiles, as the substituted surface value may still be too small for most in situ observations. To address such ambiguities when inputting a real N^2 profile, we propose a correction scheme to modify the N^2 within the mixed layer. Specifically, regarding the depth of the maximum N^2 (N^2_{mld}) as the mixed layer base, we replace the N^2 value above the mixed layer base with N^2_{mld} and use this replaced N^2 to implement the isQG experiment with the subsurface outputs (density and velocity anomalies) denoted as the original reconstructions.

After conducting a series of numerical experiments (details are referred to in Figures S2–S5 in Supporting Information S1), we find that the density reconstruction is sensitive to the modification of N^2 within the mixed layer, but velocity reconstructions are almost not. Finally, the reconstructed density anomaly is modified within the mixed layer using the following equation:

$$\rho^{\mathrm{a}}_{\mathrm{modified}}(k) = \mathrm{SSDA} + \left(\rho^{\mathrm{a}}_{\mathrm{original}}(k) - \mathrm{SSDA}\right) \times \left(\frac{N^2_{\mathrm{original}}(k)}{N^2_{\mathrm{mld}}}\right),$$

where k is the kth depth in the mixed layer, $\rho^{\mathrm{a}}_{\mathrm{original}}$ and $\rho^{\mathrm{a}}_{\mathrm{modified}}$ are the original reconstructed and modified density anomalies, respectively. N^2_{original} is the original observed N^2 profile. This modification can improve the reconstructability of the density anomaly field in the mixed layer but has little influence on deeper layers.

Both the isQG and eSQG methods consider QG-balanced ocean motions, which requires the reconstruction area to reconcile with the f-plane. In order to reconstruct the subsurface structures in the whole SIO, we first split the SIO (0°–122°E, 3°–67°S) into subregions spanning 8° in latitude and longitude on an overlapping 4° grid, and only the open ocean is retained. An open ocean is defined as no land or just a tiny area of the island in the

subregion. If the surface data are missing on the island, the values will be replaced by a weighted average of valid points around it. The weights are proportional to the inverse of the distance. Using the processed SSHA, SSDA, and N^2 as inputs, we conduct the isQG exploration in each subregion to reconstruct 3D density and velocity anomalies. Finally, reconstructions of all subregions are synthesized into the daily high-resolution (grid spacing is the same as the one of SST) fields for the SIO. Five-point weighted smoothing is applied to make a smooth transition for the reconstruction fields at the subregion boundary. Details are available in Figure S6 in Supporting Information S1.

3.2. Evaluation Method

The root mean square (RMS) value of an input x field is

$$\mathrm{RMS} = \sqrt{1/N \sum_{i=1}^{N} x_i{}^2},$$

with the summation performed along the specified dimension.

The root mean square error (RMSE) between the reconstruction field and in situ observation is

$$\mathrm{RMSE} = \sqrt{1/N \sum_{i=1}^{N} (\mathrm{observations} - \mathrm{reconstructions})^2},$$

where N is the number of observations. The reconstructed fields are spatiotemporally and linearly collocated with the in situ observations. Also, the background current, background density fields, DUACS geostrophic currents, and the GLORYS12V1 reanalysis currents are collocated similarly. The isQG vertical grids employ 57 standard depths from 0 to 1,500 m, the same as the WOA18 monthly climatology field.

The skill score (SS) is introduced from the perspective of the Lagrangian analysis to evaluate the isQG-reconstructed currents. It is computed using the methodology proposed by Y. Liu and Weisberg (2011). This nondimensional skill score indicates the relative performance of the ocean currents to the drifter observations. It has been used to evaluate several oceanic current products by Y. Liu et al. (2014) and Cancet et al. (2019). The SS is only based on the trajectories and is defined as

$$SS = \begin{cases} 1 - c, (c \le 1) \\ 0, (c > 1) \end{cases},$$

where $c = \sum_{i=1}^{N} d_i / \sum_{i=1}^{N} l_i$ is the cumulative Lagrangian separation distance (d) divided by the cumulative length of the observed drifter trajectory (l), with $i = 1, 2, \ldots, N$, $N = 3 \times 4$ is the total number of 6-hourly drifter observations in 3 days. To calculate the Lagrangian separation distance d_3, the collocated reconstructed current is first integrated to simulate the particle positions for each pseudo-drifter using a fourth-order Runge-Kutta algorithm (Y. Liu et al., 2014). Then, the Lagrangian separation distance can be measured by the relative distance between the pseudo-drifter and real drifter at the drifter position i. In this situation, $c = 0$ indicates that the performance of surface current is a perfect skill, and its corresponding SS is equal to 1 (the highest score). $c > 1$ means that the cumulative Lagrangian separation distance is larger than the observed drifter trajectory, and the surface currents would be flagged as no skill (SS = 0).

4. Results

4.1. Qualitative Analysis of a Case Reconstruction

As illustrated by the trajectory of drifter 127198, the drifter is temporally carried by a mesoscale eddy in the middle of SIO during July 2015 (Figure 2). This remarkable mesoscale phenomenon is able to demonstrate the reconstructability of the isQG method in reconstructing the structures of eddy from multisource satellite observations. We chose a reconstruction area (54°–62°E, 39°–47°S) encompassing the mesoscale eddy, with snapshots of SLA and SST on 17 July 2015, shown in Figures 3a and 3d. The notable anticyclone eddy (AE) is conspicuously

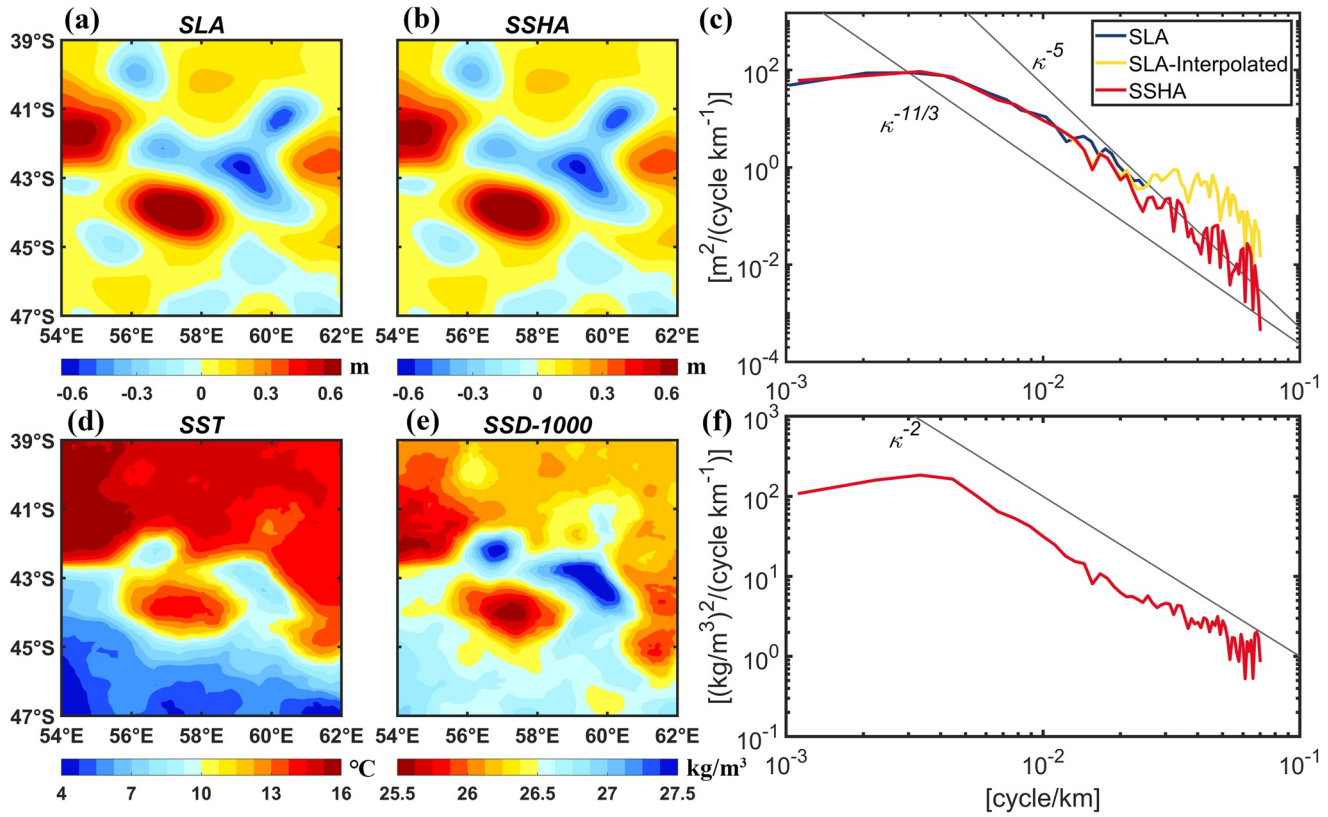

Figure 3. Snapshots of the (a) original sea level anomaly (SLA) map distributed by CMEMS, (b) preprocessed sea surface height anomaly (SSHA) map. The cut-off wavelength sets to 70 km in this situation. (c) Wavenumber spectra of the map of (a) (navy blue), the linearly interpolated higher-resolution SLA map (golden, the map is not shown here), and the map of (b) (red). Gray lines correspond to $\kappa^{-11/3}$ and κ^{-5} slopes, respectively. (d, e) Snapshots of sea surface temperature (SST) and sea surface density excess. (f) Wavenumber spectrum of sea surface density anomaly (SSDA) map, which is shown in Figure 4a. The gray line corresponds to κ^{-2} the slope. Note that the observation date of these maps is 17 July 2015.

demonstrated by SLA and SST maps around (57°E, 44°S), with positive SLA and warm core. Three cyclone eddies (CEs) are present around the AE at the same period, but their positions and shapes differ slightly between the SLA and SST maps, especially in the north area. Figure 3b illustrates a snapshot of the preprocessed SSHA, which has a higher spatial resolution and a spatial pattern compatible with the original SLA field. The differences in the spectra of the original SLA, interpolated SLA, and preprocessed SSHA maps by filtered demonstrate that directly upscaling the quarter-degree SLA map into a higher-resolution results in aliasing at the smaller scale, which may further impair the method reconstructability. Additionally, the coincidence between SST and SSD fields reveals that SST predominates the distribution of the SSD, although the SSS also modulates the density structures of the eddies (Figures 3d and 3e).

The eddy characteristics can be recognized in the SSDA and SSHA maps of the reconstruction area (Figure 4a). The SSHA field displays at least three AEs and five CEs with amplitudes ranging from ±0.7 m, and it is almost colocated with the SSDA map, particularly for the eddies at the center of the reconstruction area. In general, the correlation coefficient between SSDA and SSHA reaches −0.842 (95% significant level), which is beneficial for applying the SQG theory, according to earlier studies (Z. Chen et al., 2020; Lapeyre & Klein, 2006; L. Liu et al., 2014; J. Wang et al., 2013). Furthermore, the spectrum of the inputted SSHA map displays a slope between $\kappa^{-11/3}$ and κ^{-5}, while the SSDA spectrum follows a shallow slope with κ^{-2}(Figures 3c and 3f). These spectra are closer to the SQG-like regime that highlights the frontal dynamics and dominates the surface dynamics (Capet et al., 2008; Klein & Lapeyre, 2009; Sasaki & Klein, 2012). It is also worth noting that the high-resolution SST map used in this study allows the SSDA field to reasonably resolve a smaller-scale process (beyond about 30 km) surrounding the temperature fronts and mesoscale eddies (Figure 3f).

With the SSHA, SSDA, and N^2 fields presented in Figure 4, the 3D density and velocity anomalies can be reconstructed using the isQG method. Figures 5a–5c depict the near-surface background velocity, reconstructed

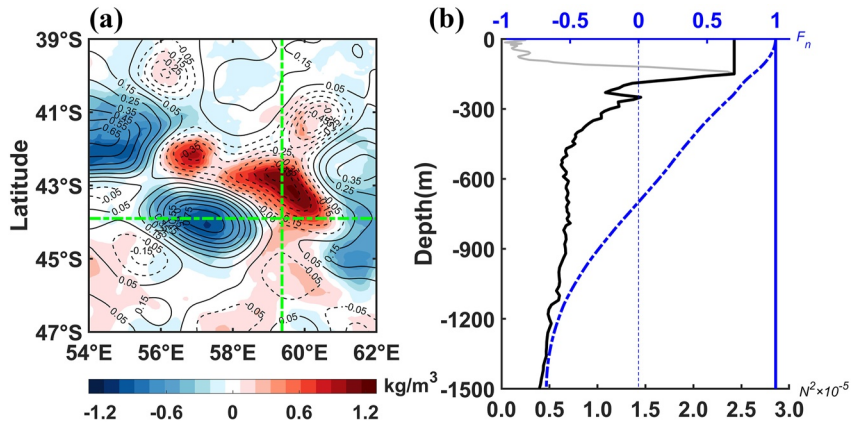

Figure 4. (a) Snapshots of the sea surface density anomaly (SSDA; shading, unit: kg/m^3) and sea surface height anomaly (SSHA; contour, unit: m) on 17 July 2015. Green dash-dot lines show the location of the vertical profiles in Figure 6. (b) Vertical profile of the original regional averaged N^2 (gray line), the inputted modified N^2 (black line), and barotropic (solid blue line) and first baroclinic modes (dash-dot blue line).

velocity anomaly at 15 m, and the total velocity at 15 m (sum of the above two terms) in the reconstruction area, respectively. The background velocity primarily flows from west to east with amplitudes smaller than 0.3 m/s due to the reconstruction area's location between the tail of Agulhas Return Current and Antarctic Circumpolar Current (Figure 5a). At the moment, the local currents are dominated by substantial mesoscale signals, resulting in strong flows around the eddies and meander with amplitudes of more than 0.85 m/s. The direction and amplitude of the currents are determined by the SSHA map distribution and modulated by temperature fronts (Figure 5b). The background velocity locally modulates the eddy-induced velocity anomaly in velocity structure and amplitude, such as increasing (decreasing) the velocity amplitudes at the south (north) edge of the strongest AE, revealed by the distribution of the total velocity field at 15 m depth (Figure 5c).

Figures 5d–5f present the reconstructed density and velocity anomalies at depths of 15, 250, and 500 m, respectively. Additionally, Figures 5g and 5h comprehensively investigate the wavenumber spectrum analysis of these fields. Our results demonstrate that the high-resolution density and velocity anomalies are reasonably reconstructed using multisource observations at different depths (Figures 5d–5f). Furthermore, inputting the higher-resolution SST observation has led to a tolerable resolution of scales larger than about 30 km and improved the effective resolution of the reconstructed fields. The amplitudes of the velocity anomaly gradually decrease with increasing depth, quantified through the variation of KE spectra at different depths. At the 15 m depth, the KE spectrum of the total velocity is highly similar to that of the velocity anomaly at most scales, emphasizing the dominance of mesoscale eddies in the upper ocean dynamics at this moment. At 250 and 500 m, the KE spectra gradually drop following a slope between k^{-2} and k^{-3} for scales from 300 to 30 km, consistent with the SQG regime (Figure 5g). Regarding density reconstruction, the SSDA primarily affects shallow layers. Our proposed modification is necessary and beneficial within the mixed layer. At deeper layers, the density anomaly remains highly correlated with the velocity anomaly and is regulated by SSDA and SSHA. Furthermore, the reduction of density anomaly with depth can be quantified through the value of their spectra at various depths.

Figure 6 shows the vertical structures of the strong mesoscale eddies. The west-east profile crosses the aforementioned strongest AE along 44°S (Figure 6a), and the south-north profile partially crosses the strongest CE along 59.4°E (Figure 6b). Both AEs and CEs exhibit bowl-shaped density anomalies with maximum values at the base of the mixed layer. The density anomalies increase from the surface to the mixed layer depth, with the maximum RMS reaching 0.69 kg/m^3, then decreasing with increasing depth, reducing by 0.3 kg/m^3 at about 400 m. Notably, the AE has a deeper density anomaly than the adjacent CE (Figure 6a), while the CE's density anomaly reduces more rapidly at the upper layers (Figure 6b). Regarding the velocity anomaly, the AE's spatial shape is approximately elliptical along 43.9°S, resulting in symmetrically distributed meridional velocity anomalies (v_a) with opposing amplitudes. The maximum velocity anomaly is higher than 0.8 m/s, distributed between the eddy center and the utmost boundary. At the surface, the RMS of v_a is 0.43 m/s, decreasing steadily to less than 0.1 m/s at 800 m depth (Figures 6a and 6c). On the other hand, the CE's spatial shape is irregular along 59.4°E, resulting

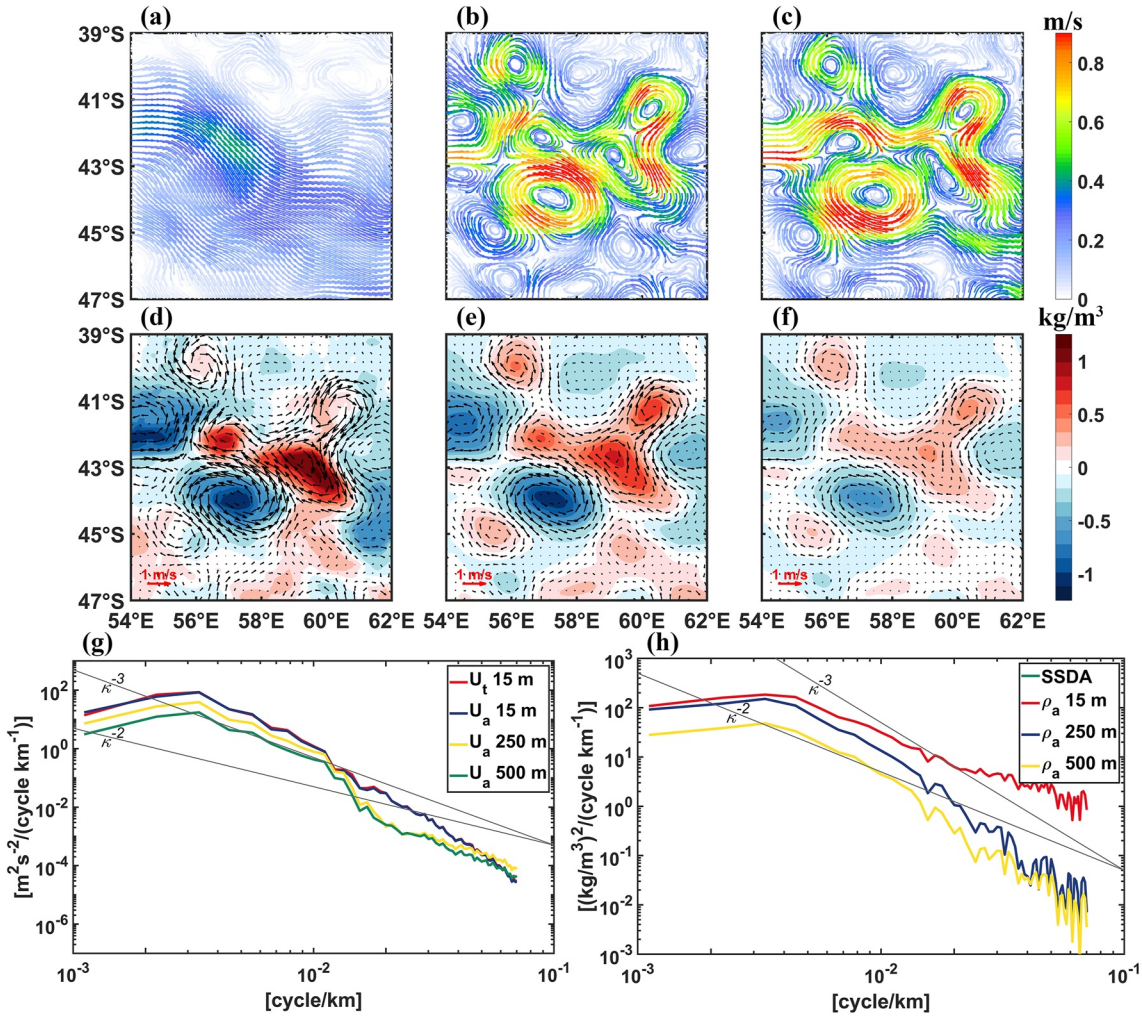

Figure 5. Snapshots of (a) the near-surface background velocity, (b) reconstructed velocity anomaly at 15 m, (c) the total velocity at 15 m. Curve arrows and colors show the velocity direction and amplitude (unit: m/s). (d–f) Reconstructed density (shading, unit: kg/m^3) and velocity (quiver, unit: m/s) anomalies at depths of 15, 250, and 500 m, respectively. Vectors are plotted every three grid points. (g, h) Wavenumber spectra of the reconstructed fields of (c)–(f). Gray lines correspond to κ^{-3} and κ^{-2} slopes. Note that the density anomaly at 15 m depth covers the wavenumber spectrum of sea surface density anomaly (SSDA; green line) due to their almost the same characteristics. The date of these snapshots is 17 July 2015.

in an asymmetry of the zonal velocity anomaly (u_a). The south edge of the CE flows faster than its north edge on the whole, and this asymmetry is captured by our reconstruction method. The RMS of u_a steadily drops from 0.23 m/s to almost nil from the sea surface to deeper layers along the entire vertical profile (Figures 6b and 6c).

Based on the above results, we conclude that with some modifications, the isQG method holds promise for reconstructing the 3D density and velocity fields of eddies by utilizing multisource satellite observations. The reconstructed fields reasonably capture the smaller-scale processes generated by temperature fronts by inputting a higher-resolution SST map. However, due to the lack of contemporaneous subsurface observations near the reconstruction area, the quantitative analysis of this case study cannot be fully supported. As a result, in Section 4.2, our focus will be on quantitatively evaluating the reconstructed fields using independent observations.

4.2. Quantitative Evaluation of the Reconstruction Fields

We initially rely on drogued drifter velocities to evaluate the reconstructed shallow-layer velocity field. The drifter 127198 is chosen as a benchmark for the following reasons: first, its movement is associated with four significant currents in the SIO—the Agulhas Current, Agulhas Return Current, South Indian Current, and Antarctic Circumpolar Current. Additionally, it was captured by the aforementioned strong AE for at least a week, making

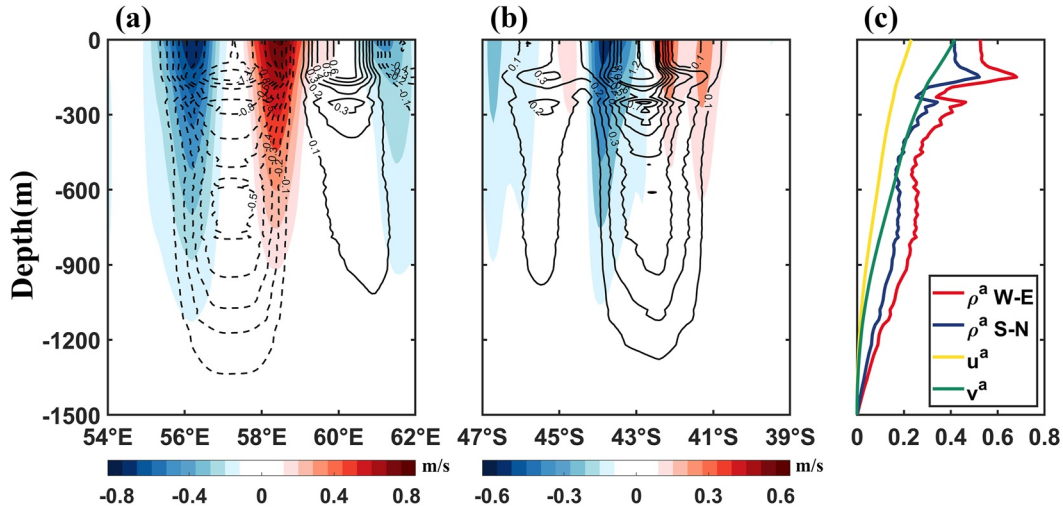

Figure 6. (a) Vertical profile of density anomaly (contour) and velocity anomaly (shading) along the west-east direction green dash-dot line in Figure 4 on 17 July 2015. (b) As in (a), but for the south-north direction. (c) Vertical profile of root mean squares (RMSs) of density and velocity anomalies.

it an excellent representative for estimating the interactions between background flows and eddies in the SIO. Second, its drogued life extends beyond 5 months, providing a long-term observation record that yields statistically significant results.

Figures 7 and 8 present the quantitative evaluations of velocity fields at 15 m depth by considering the correlation coefficient (95% significance), standard deviation, RMSE, and skill score. The reconstructed velocities, including the zonal and meridional components and their corresponding velocity phase, show strong pattern correlations with the observations, with correlation coefficients as high as 0.959, 0.941, and 0.716, respectively (Figure 7). These results demonstrate that our reconstructed velocity captures the near-surface current changes over the observation period, supported by the qualitative analysis of the time series graphs (referred to in Figure S7 in Supporting Information S1). The amplitude of the reconstructed zonal component is 26.3 ± 43.9 cm/s, which is weaker than that of observation (32.9 ± 61.9 cm/s), and this difference generates a 23.1 cm/s RMSE between the reconstructed and observed zonal components. This feature is also shown in the meridional component, but by contrast, the zonal component is better reconstructed than the meridional counterpart. Regarding the velocity phase, the standard deviation of reconstructed velocity is comparable to that of the observation, with an RMSE of 53.4° between them (Figure 7). Further, utilizing the above velocities, the skill score of the reconstructed

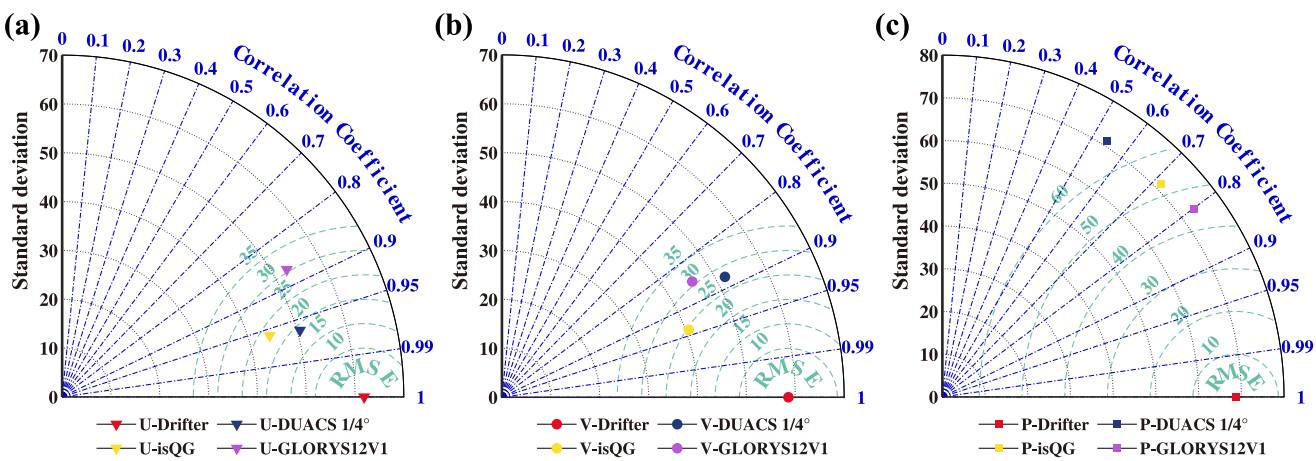

Figure 7. Taylor diagram for (a) zonal and (b) meridional velocity components (unit: cm/s) and (c) velocity phase of the drifter observation (red), interior + surface quasigeostrophic (isQG)-reconstructed currents (golden), Data Unification and Altimeter Combination System (DUACS) geostrophic currents (navy blue), and GLORYS12V1 reanalysis currents (purple), respectively. The correlation coefficients are at 95% significance.

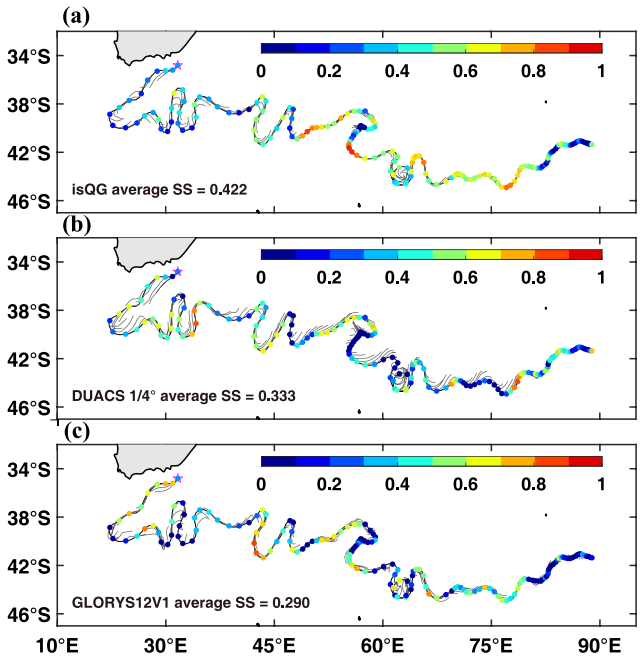

Figure 8. (a) The skill score (colored circle) of the interior + surface quasigeostrophic (isQG)-reconstructed currents on each Julian day. Magenta five-pointed star is the observation starting point of the drifter 127198. The black line is the original trajectory of the drifter from 13 April 2015 to 27 September 2015. The gray line is the virtual trajectory simulated by reconstructed velocities on each Julian day. (b, c) As in (a), but for the Data Unification and Altimeter Combination System (DUACS) geostrophic currents, and the GLORYS12V1 reanalysis currents, respectively.

velocities can be calculated on each Julian day (Figure 8a). Over the whole observation period, the skill score averages 0.422, indicating a relatively high score (Cancet et al., 2019; Y. Liu et al., 2014). In particular, the skill scores are mostly higher than 0.5 near 60°E in July 2015 when the strong AE caught the drifter, suggesting that the reconstructed velocity performs well in describing the eddy velocities. Regions with lower skill scores are typically eddy poor or the strong western current system (Ding et al., 2022), where the drifter may occasionally be affected by high-frequency ageostrophic processes.

The reconstructed surface currents are also validated compared with other established surface current data sets, including the DUACS geostrophic currents, and the GLORYS12V1 reanalysis currents. In contrast to the DUACS surface geostrophic currents, our reconstructed currents enhance the reconstructability of the velocity phase by the improvement of the velocity meridional component. On average, the skill score of the reconstructed currents surpasses that of the geostrophic currents by 0.089, with notably higher values east of 40°E (Figures 7 and 8b). Additionally, the GLORYS12V1 surface currents exhibit the lowest average skill scores among the three current data sets, with an average score of 0.290, due to the overestimation of velocity amplitudes for both zonal and meridional components compared to drifter observations (Figures 7 and 8c).

To evaluate the reconstructed subsurface currents, the high vertical resolution subsurface velocity and thermohaline profiles from one of the GO-SHIP observations (ExpoCodes: 33RR20090320, north-west direction observation in Figure 2) is used. The observed velocity amplitudes in this cruise were briefly introduced in the cruise summary report (see Figure 1 in the Lowered Acoustic Doppler Current Profiler section of the cruise scientific report at https://cchdo.ucsd.edu/cruise/33RR20090320).

The reconstructed velocity field revealed four significant aspects along the west-to-east section (Figure 9). During the initial phase of the cruise, the reconstructed anomalous zonal component values display a pattern of positive to negative variation, with peak values of around 16 cm/s near the surface, which decrease as depth. Correspondingly, the anomalous meridional component values demonstrate a positive–negative–positive–negative pattern, with values similar to those of the zonal component. This feature is consistent with the cruise passing through the south and north margins of two adjacent AEs between 30° and 38°E after briefly crossing the southwesterly Agulhas Current. Further to the east, a CE is demonstrated at the center of the Mozambique Basin, where the horizontal velocities reach a maximum of 17.6 cm/s in the middle of the water column. The meridional component shows opposite flow directions on the west and east sides of 40°E. At approximately 55°E, 88°E, and 101°E, various types of eddies are present at the upper layers of the well-known ocean ridges. Even though the sea level fluctuations in these eddies are small, the anomalous subsurface velocities were between 10 and 30 cm/s around the eddy cores. Finally, the cruise reached the western coast of Australia, which is also regarded as an eddy-rich area (Ding et al., 2022). The eddy activities on the west side of the Leeuwin Current were weak at the time, but our reconstructed velocities effectively capture them. These pronounced features are also captured by the cruise observations (Figures 9d and 9e), which further affirms the reliability of our reconstruction framework in describing the velocity field within eddy-rich regions.

Subsequently, we utilized two independent GO-SHIP cruises, namely 33RR20090320 and 33RR20160208, to further evaluate the reconstructed density field. These cruises provide continuous, long-term T/S profile observations that are essential for evaluating density anomalies. Figure 10 shows the reconstructed (Figure 10b) and observed (Figure 10c) density anomalies, as well as the associated isopycnal curve (Figure 10d), from the cruise 33RR20090320 in depth–longitudinal sections. The reconstructed density anomaly, which ranges from −0.732 to 0.754 kg/cm^3, portrays the vertical structures of the observed stronger eddies. The correlation coefficient and RMSE between reconstructed and observed density anomalies are 0.575 and 0.148 kg/cm^3 for the entire sections, respectively. However, considering depths deeper than 100 m, the correlation value increases to 0.592.

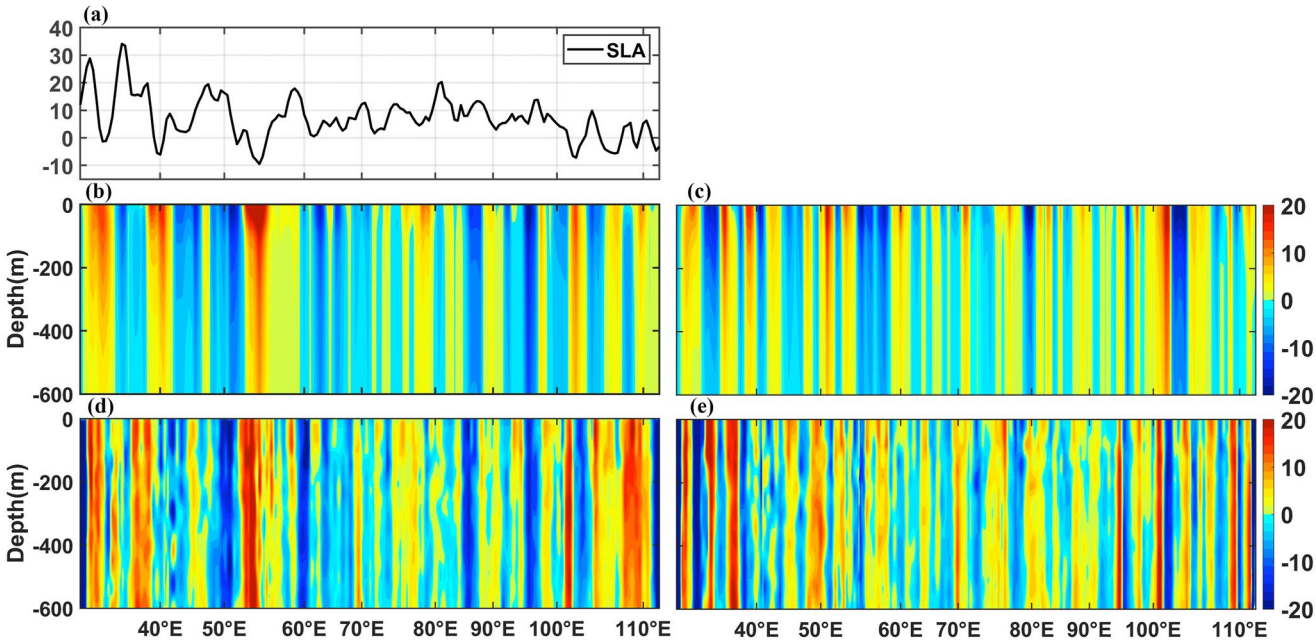

Figure 9. (a) Sea level anomaly (SLA; unit: cm) along the GO-SHIP observation (ExpoCodes:33RR20090320, north-west direction observation in Figure 2). The daily, gridded SLA map is interpolated at the location and time of each cruise observation station. (b, c) Reconstructed zonal and meridional velocity (unit: cm/s) depth–longitudinal sections. (d, e) As in (b) and (c), but for the GO-SHIP observation. The figure is cited from Figure 1 in the Lowered Acoustic Doppler Current Profiler section of the cruise scientific report at https://cchdo.ucsd.edu/cruise/33RR20090320. The observation date is from 25 March to 10 May 2015.

Notably, the reconstructed field agrees better with the observed one in deeper layers, while the reconstruction difference concentrates on eddy-poor areas and depths shallower than 100 m. By modifying the density anomaly within the mixed layer, we are able to attenuate the reconstruction errors while also successfully reproducing partial structures of subsurface-intensified eddies in the middle of the SIO. Furthermore, the reconstructed density excess aligns with the isopycnal curves larger than 26 kg/m^3 observed in real observation, demonstrating the ability of the reconstructed density field to depict variations in the pycnocline (Figure 10d). Despite these achievements, some reconstruction errors remain, which may be attributed to unknown high-frequency signals that are beyond the current capabilities of our method (Figures 10b, 10c, and 12a). However, since contemporaneous SSS observations are unavailable during this cruise, uncertainties in modifying density anomalies within the mixed layer may have led to less accurate density reconstructions in upper layers (Figure 12a).

Figure 11 shows the same contents as Figure 10, except for the later cruise 33RR20160208. The exploration of cruise 33RR20160208 began in the Antarctic Ocean, then transited the Antarctic Circumpolar Current and South Indian Current from 8 February to 16 March 2016 (see the south-north direction GO-SHIP observation in Figure 2). Here, we focus on the thermohaline observations obtained from 60°S to the end of the cruise. The reconstructed density anomaly exhibits improved agreement with the observed field along this section, with an overall correlation coefficient of 0.755 and an RMSE of 0.075 for depths deeper than 100 m. Moreover, the reconstruction errors are concentrated mainly within depths shallower than 100 m (see Figures 11b, 11c, and 12b). Several factors contribute to the improvement in the reconstruction fields. Regarding regional dynamics, eddies are primarily generated by baroclinic instability caused by thermohaline variations in the mid-to-high latitudes of the interior ocean. The dynamics in these areas are significantly influenced by vertical barotropic and the first baroclinic modes, which can be effectively characterized by the SQG theory (Z. Chen et al., 2020). Therefore, the dynamic characteristics of the regions traversed by the cruise determine the better reconstruction. Additionally, using satellite-observed SSS enhances the accuracy of the observed SSD, promoting a better estimate of the density anomaly at shallower layers.

In addition, beyond the reconstruction errors attributed to the reconstruction method and regional dynamics, another potential source of reconstruction error stems from the SST observation itself. Despite considerable effort presently being devoted to producing high-resolution SST analyses with a goal of spatial grid resolutions as low as 1 km, the effective resolution of the generated SST fields has not been proportionately improved,

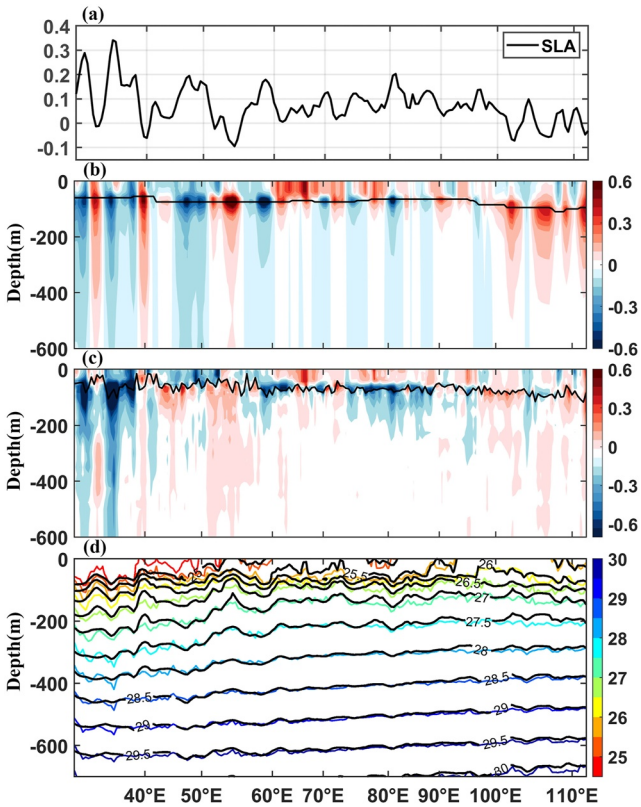

Figure 10. (a) Sea level anomaly (SLA; unit: m) along the GO-SHIP observation (ExpoCodes:33RR20090320, north-west direction observation in Figure 2). The daily, gridded SLA map is interpolated at the location and time of each cruise observation station. (b, c) Reconstructed and observed density anomalies (unit: kg/m^3) depth–longitudinal sections, respectively. Black lines denote the depth of mixed layer base computed from ISAS-ARGO and GO-SHIP profiles around observation stations, respectively. (d) Observed (color contour) and reconstructed (black contour) isopycnal curve depth–longitudinal section (unit: kg/m^3). The cruise observation date is from 25 March to 10 May 2015.

particularly during periods when high-resolution infrared SST sensors are occluded by clouds in the eddy-active areas (Reynolds et al., 2013). This leads to a temporal variation of the effective spatial resolution of SST products in an unphysical manner, artificially suppressing smaller scales during cloudy periods (Fiedler et al., 2019). Consequently, small-scale near-surface ocean dynamics reconstruction may be underpredicted or overestimated, introducing additional errors in the reconstruction structures. Our additional uncertainty trials, although not included in this study, support the fact that regions with higher quality level observations from infrared SST sensors demonstrate an enhanced effective resolution. It is worth noting that the results indicate that MWIRSST performs better in resolving smaller-scale signals despite its ∼1/10° grid spacing. Conducting more sensitive experiments would be valuable in quantifying the impact of reconstruction errors caused by cloud cover when applying the reconstruction method.

5. Conclusion and Discussion

In light of the sparse observations of the oceanic subsurface, particularly in the SIO, reconstructing the 3D structure of evolving mesoscale eddies remains a challenge in oceanography. This study explores the potential of reproducing the 3D structures of mesoscale eddies based on satellite-based observations. We first apply the isQG method to estimate the ocean subsurface density and velocity fields based on multisource observations to achieve this. The input data for the isQG method include the moderate-resolution (1/4°) SSH-gridded field, higher-resolution (∼1/10°) RMESS SST, satellite-based SSS, and an estimate of vertical stratification from Argo-based monthly fields. To enhance the effective resolution of the reconstructed 3D structures, we introduce the higher-resolution SST image to compensate for the relatively lower effective temporal resolution of the SSH map. As a result, a preprocessing scheme is suggested to incorporate the different resolution SST/SSH/SSS data based on the frameworks of geostrophic approximation and the eSQG method. On the other hand, considering the limitations of the isQG method within the mixed layer, we propose a modification scheme to improve the reconstructability of density at the upper layers. The suggested correction scheme enhances the stability of the density reconstruction at shallow depths and rectifies the deficiency of the isQG method.

The reconstructed subsurface structures of a notable AE are scrutinized in the middle of SIO at first. The snapshot results show that the isQG method is capable of reconstructing the high-resolution subsurface density and velocity fields of eddies at various depths using multisource satellite observations. Spectra analysis reveals that our reconstructed velocity fields follow a κ^{-2} and κ^{-3} slope consistent with the SQG regime for 300–30 km scales at different depths. Our method effectively enhances the resolution of the reconstructed fields, capturing rapidly evolving processes associated with temperature fronts. The reconstructed density and velocity anomalies also depict the asymmetry degradation rate of velocity anomaly on both sides of the AE or CE with an increasing depth. Subsequently, emphasis has been placed on the quantitative evaluation of long-term reconstructed fields using independent observations from drogued drifter and GO-SHIP T/S profiles. Our reconstructed velocity fields show better agreement with in situ observations of eddy-active areas, and the primary structure of the eddy-induced velocity anomaly can be reproduced.

Regarding the density reconstruction, our suggested correction scheme within the mixed layer improves the stability of the density reconstruction at shallower layers. At depths deeper than 100 m, the isQG method's reconstructability remains high caliber at most moments. Overall, our analyses are anticipated to support the eddy's 3D structures reconstruction at mid-to-high latitudes in the SIO, in which the evolution of eddies may be sufficiently explained by the thermohaline variation-generated baroclinic instability, merit-enhanced reconstructability applying the isQG method. The above results reveal that incorporating higher-resolution satellite

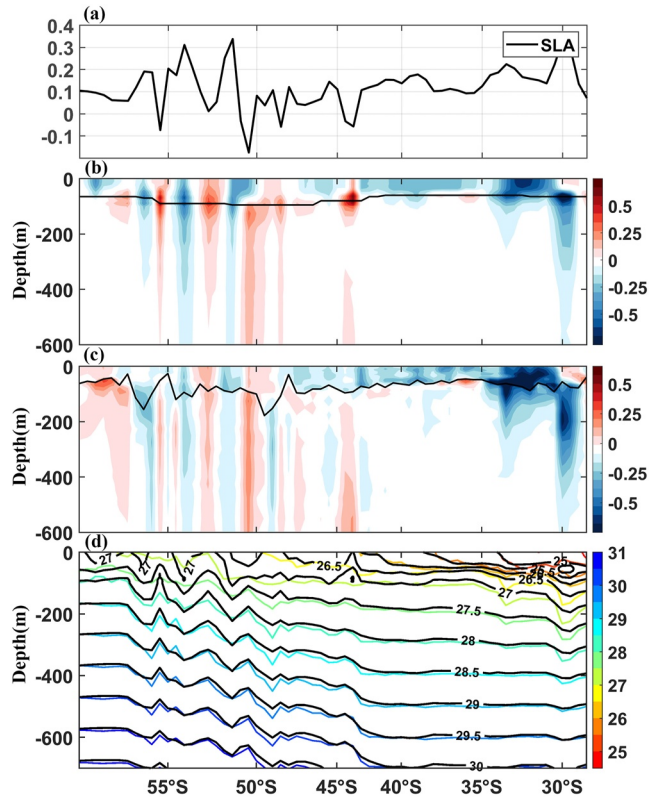

Figure 11. (a) Sea level anomaly (SLA; unit: m) along the GO-SHIP observation (ExpoCodes:33RR20160208, south-north direction observation in Figure 2). The daily, gridded SLA map is interpolated at the location and time of each cruise observation station. (b, c) Reconstructed and observed density anomalies (unit: kg/m^3) depth–latitudinal sections, respectively. Black lines denote the depth of mixed layer base computed from ISAS-ARGO and GO-SHIP profiles around observation stations, respectively. (d) Observed (color contour) and reconstructed (black contour) isopycnal curve depth–latitudinal section (unit: kg/m^3). The cruise observation date is from 19 February to 11 March 2016.

measurements into the reconstruction study of evolving eddy 3D structures is a promising strategy, which will aid the next steps in understanding, constructing, and constraining eddy. However, it should be noted that cloud cover is more prevalent in the mid-to-high latitudes of the SIO (Reynolds et al., 2013), which may affect the effective resolution of the gridded SST observation and introduce potential sources of error in the reconstructed fields. Therefore, additional prevalidation of the quality of the SST information is warranted in practical application. Furthermore, by incorporating SST information, extensive efforts have been dedicated to enhancing the spatial–temporal resolution of SMOS SSS observations from 1/4° every 4 days to 1/20° daily. Its resultant effective resolution still faces challenges in matching that of SST. More consideration warrants discussing the potential risks of using different SSS products in real applications.

Although the present reconstruction results demonstrate encouraging reconstructability using the isQG method with the surface inputs from satellite observation, some challenges warrant explorations. It is difficult for a few smaller-scale motions and high-frequency signals to be resolved by the current satellite observations, even the SST observations. Such observation limitation struggles the isQG method to reconstruct the subsurface structures of the majority of smaller-scale motions, resulting in a smoother vertical section of the reconstructed current compared to the observed ones (Figure 9). With advancements in satellite observation techniques or the application of deep (machine) learning methods (e.g., S. A. Martin et al., 2023), the effective resolution of satellite-observations may be improved, which would partly reduce the bias of the reconstructed fields. Besides, the upcoming higher-resolution surface information would bring the signals of some unbalanced motions or high-frequency signals (Morrow et al., 2019) that cannot be handled by the SQG framework. It will be desirable to figure out how to additionally quantify the contributions of unbalanced motions or high-frequency signals in the upper ocean when merging the high-resolution surface information in the future (e.g., Archer et al., 2022; Buongiorno Nardelli et al., 2018; Torres et al., 2022; Ubelmann et al., 2021, 2022).

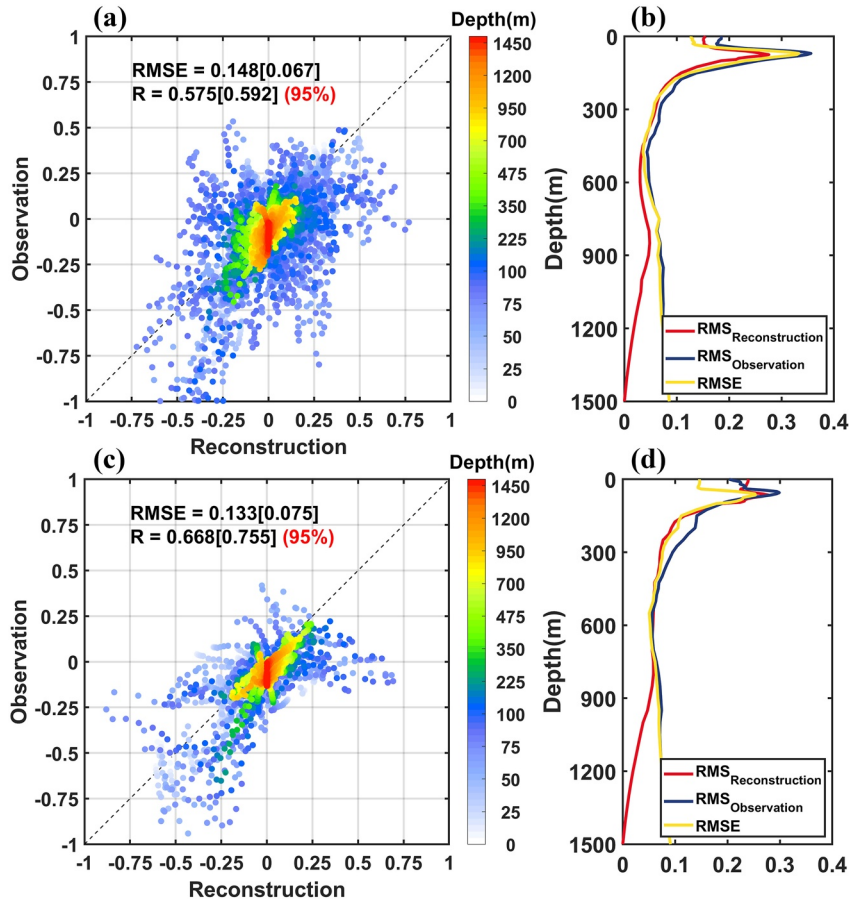

Figure 12. (a) Density anomalies (unit: kg/m^3) of observed (cruiseExpoCodes:33RR20090320, *y*-axis) and reconstructed field (*x*-axis) at the 57 standard depths. The standard depths are the same as the WOA18 monthly climatology fields. The RMSE and *R* are root mean square error and correlation coefficient between observed and reconstructed density anomalies, respectively. The square bracket represents the statistic result below 100 m. The red parenthesis represents the 95% significant level. (b) The vertical profiles of root mean square (RMS) of the reconstructed (red) and observed (dark blue) density anomalies and the corresponding RMSE between them (golden), respectively. (c, d) As in (a) and (b), but for the observations provided by cruise 33RR20160208.

Moreover, the present isQG method remains some limitations. The isQG method only employs the barotropic and the first baroclinic modes to reproduce the subsurface structures, which may result in the reconstructed velocity and density fields systematically being more surface intensified than in the observations at shallower depths. Therefore, one possible way is introducing additional baroclinic modes in the interior solution of the isQG method to fully represent the ocean interior, as suggested by L. Liu et al. (2019). Alternatively, implementing the SQG-based dynamical–statistical framework (as proposed by Yan et al. [2020]) to mitigate surface-intensified reconstruction structures is worth considering. Lastly, using high-quality daily vertical stratification profiles, particularly when subsurface observations are sufficient, may enhance the method's performance. The inclusion of daily vertical stratification ensures a more accurate presentation of the density anomaly reconstructions within the mixed layer.

Appendix A: Theoretical Background of the isQG and eSQG Methods

In the quasigeostrophic theory, the stream function and PV are related (Hoskins, 1975):

$$\left(\nabla^2 + \frac{\partial}{\partial z}\frac{f_0^2}{N^2}\frac{\partial}{\partial z}\right)\psi = Q(x, y, z, t);\ \nabla^2 = \frac{\partial^2}{\partial x^2} + \frac{\partial^2}{\partial y^2}, \tag{A1}$$

where $\psi = p(\rho_0 f_0)^{-1}$ is the geostrophic stream function; p, ρ_0, and f_0, respectively, are the pressure anomaly, reference density, and Coriolis factor; $N^2(z) = -(g/\rho_v)\left(\partial\overline{\rho}/\partial z\right)$ is the squared buoyancy frequency; ρ_v is the volumetric mean of potential density; and $\overline{\rho}$ is the horizontal average of potential density in the study region. Q is the quasi-geostrophic potential vorticity (QGPV) anomaly (Pedlosky, 1987).

Due to the linearity of the QGPV equation, the total stream function ψ in Equation A1 can be decomposed into a homogeneous solution termed the SQG solution ψ^{sur} and a particular solution called the interior solution ψ^{int} (Lapeyre, 2009; L. Liu et al., 2019; J. Wang et al., 2013). Under approximate boundary conditions, Equation A1 can be decomposed into

$$\left(\nabla^2 + \frac{\partial}{\partial z}\frac{f_0^2}{N^2}\frac{\partial}{\partial z}\right)\psi^{sur} = 0,$$
$$f_0\frac{\partial\psi^{sur}}{\partial z}|_{z=0} = b_s,\ \lim_{z\to -H}\frac{\partial\psi^{sur}}{\partial z} = 0, \tag{A2}$$

$$\left(\nabla^2 + \frac{\partial}{\partial z}\frac{f_0^2}{N^2}\frac{\partial}{\partial z}\right)\psi^{int} = Q,$$
$$\frac{\partial\psi^{int}}{\partial z}|_{z=0,-H} = 0, \tag{A3}$$

where $b_s = -g\rho'/\rho_0$ is the buoyancy anomaly, g is the gravity constant, ρ' is the density anomaly, and ρ_0 is the reference density. Equations A1 and A2 and the combination of them represent the classic Eady model, QG model, and Charney-like mode, respectively. Equation A1 can be directly solved by inputting the b_s and N^2, but the solution of Equation A2 needs more assumptions to derive indirectly because of unknown Q.

A1. The isQG Method

J. Wang et al. (2013) numerically solved Equation A1 by using the finite-difference method to look for the ψ^{sur}. The equation was discretized on an equally spaced staggered grid (details are shown in the Appendix of their paper) and then truncated ψ^{int} to the two gravest (BT and BC_1) modes:

$$\hat{\psi}^{int}(k,l,z) = \sum_m A_m(k,l)\mathbb{S}_m(z) \approx A_0(k,l)\mathbb{S}_0(z) + A_1(k,l)\mathbb{S}_1(z), \tag{A4}$$

where the hat denotes the horizontal Fourier transform, (k,l) are horizontal wavenumbers. The term $\mathbb{S}_m$ is the traditional flat bottom normal mode with A_m the modal coefficient. The key point of the isQG method is that both ψ^{sur} and ψ^{int} contribute to SSHA (η) and bottom pressure (assuming zero), such that

$$\hat{\psi}^{int}(k,l,0) = A_0\mathbb{S}_0(0) + A_1\mathbb{S}_1(0) = \frac{g}{f_0}\hat{\eta} - \hat{\psi}^{sur}(k,l,0),$$
$$\hat{\psi}^{int}(k,l,-H) = A_0\mathbb{S}_0(-H) + A_1\mathbb{S}_1(-H) = -\hat{\psi}^{sur}(k,l,-H). \tag{A5}$$

The amplitudes of the two gravest modes, A_0 and A_1 are determined by Equation A5, and then we obtain the $\hat{\psi}^{int}$ and the total solution $\hat{\psi}$. Finally, the ψ is calculated by an inverse Fourier transform in horizontal space of $\hat{\psi}$, and the density and velocity anomalies can be diagnosed from the ψ as follows:

$$\rho^a = -\rho_0 f g^{-1}(\partial\psi/\partial z), \overrightarrow{V}^a = \vec{z}\times\nabla\psi. \tag{A6}$$

A2. The eSQG Method

For obtaining the SQG solution ψ^{sur}, the eSQG method employed a constant stratification ($N_0 = n_0 f_0$, with n_0 being the Prandtl ratio determined by Tulloch and Smith (2006), N_0 is the average of N^2 upper 500 m), and then analytically solved Equation A2 as (Isern-Fontanet et al., 2008; Lapeyre & Klein 2006)

$$\hat{\psi}^{sur}(k,l,z) = \frac{\hat{b}_s(k,l,0)}{N_0\kappa}\exp\left(\frac{N_0\kappa z}{f_0}\right), \tag{A7}$$

where $\kappa = \left(k^2 + l^2\right)^{1/2}$ is the modulus of the wavenumber vector.

Based on the assumption that the interior PV and SSDA are well correlated, the eSQG method approximates the total solution ψ as follows:

$$\hat{\psi}(k,l,z) = \frac{\hat{b}_s(k,l,0)}{f_0 n_b \kappa}\exp(n_0 \kappa z). \tag{A8}$$

The n_b is an empirically obtained effective Prandtl ratio that considers the interior PV's contribution. Details for the derivation of Equations A7 and A8 can be found in Isern-Fontanet et al. (2008).

In this study, we suggest using the following equation to substitute Equation A5 while solving the SQG equations:

$$\begin{aligned}\hat{\psi}^{\text{int}}(k,l,0) = A_0\mathbb{S}_0(0) + A_1\mathbb{S}_1(0) = \frac{g}{f_0}\hat{\eta}\,|_{\kappa\le 2\pi/L_c} + \frac{\hat{b}_s}{f_0 n_b \kappa}|_{\kappa>2\pi/L_c} - \hat{\psi}^{\text{sur}}(k,l,0),\\ \hat{\psi}^{\text{int}}(k,l,-H) = A_0\mathbb{S}_0(-H) + A_1\mathbb{S}_1(-H) = -\hat{\psi}^{\text{sur}}(k,l,-H).\end{aligned} \tag{A9}$$

This step aims to ensure that the low-pass processes do not affect the KE spectrum of the reconstructed velocity at scales smaller than L_c in the upper layer. The definition of L_c refers to Figure S1 in Supporting Information S1.

Data Availability Statement

We are grateful for the freely available data for this paper: SLA and DUACS geostrophic current are available from the Copernicus Marine Service (2023a); MWIRSST product is produced by Remote Sensing Systems (2023); the SMOS-BEC SSS product is distributed by the Barcelona Expert Center (2023); the MDT is available from the Copernicus Marine Service (2023b); the ISAS20-ARGO T/S fields are produced by SEANOE (2021); the drogued drifter velocities are distributed by National Oceanic and Atmospheric Administration Atlantic Oceanographic and Meteorological Laboratory (2023); the GO-SHIP subsurface velocity and T/S profiles are distributed by CLIVAR and Carbon Hydrographic Data Office (2023) and National Centers for Environmental Information (2023) produces the WOA monthly climatology T/S fields. The currents from GLORYS12V1 are available from the Copernicus Marine Service (2023c).

Supporting Information S1 and the codes to reproduce our reconstructions and figures are all available in a Zenodo repository (Z. Chen et al., 2023). The figures displayed in this study are generated using MATLAB (The MathWorks Inc, 2022).

Acknowledgments

Constructive comments by three anonymous reviewers helped improve an early version of the manuscript. This study is supported by the National Natural Science Foundation (41776004 and 41876224), the Fundamental Research Funds for the Central Universities (B210203041), the Opening Project of Key Laboratory of Marine Environmental Information Technology (20195052912), and the China Ocean Mineral Resources Research and Development Association Program (DY135-E2-3-02). Zhiqiang Chen was also supported by the scholarship from China Scholarship Council (Grant 202206710079).

References

Arbic, B. K., Polzin, K. L., Scott, R. B., Richman, J. G., & Shriver, J. F. (2013). On eddy viscosity, energy cascades, and the horizontal resolution of gridded satellite altimeter products. *Journal of Physical Oceanography*, *43*(2), 283–300. https://doi.org/10.1175/JPO-D-11-0240.1

Archer, M. R., Li, Z., Wang, J., & Fu, L. (2022). Reconstructing fine-scale ocean variability via data assimilation of the SWOT pre-launch in situ observing system. *Journal of Geophysical Research: Oceans*, *127*, e2021JC017362. https://doi.org/10.1029/2021JC017362

Ballarotta, M., Ubelmann, C., Pujol, M.-I., Taburet, G., Fournier, F., Legeais, J.-F., et al. (2019). On the resolutions of ocean altimetry maps. *Ocean Science*, *15*(4), 1091–1109. https://doi.org/10.5194/os-15-1091-2019

Barcelona Expert Center. (2023). Global SMOS SSS maps [Dataset]. https://doi.org/10.5194/essd-13-857-2021

Beal, L. M., & Bryden, H. L. (1997). Observations of an Agulhas undercurrent. *Deep Sea Research Part I: Oceanographic Research Papers*, *44*(9–10), 1715–1724. https://doi.org/10.1016/S0967-0637(97)00033-2

Beal, L. M., De Ruijter, W. P. M., Biastoch, A., Zahn, R., & SCOR/WCRP/IAPSO Working Group 136. (2011). On the role of the Agulhas system in ocean circulation and climate. *Nature*, *472*(7344), 429–436. https://doi.org/10.1038/nature09983

Biastoch, A., Böning, C. W., & Lutjeharms, J. R. E. (2008). Agulhas leakage dynamics affects decadal variability in Atlantic overturning circulation. *Nature*, *456*(7221), 489–492. https://doi.org/10.1038/nature07426

Biastoch, A., Durgadoo, J. V., Morrison, A. K., van Sebille, E., Weijer, W., & Griffies, S. M. (2015). Atlantic multi-decadal oscillation covaries with Agulhas leakage. *Nature Communications*, *6*(1), 10082. https://doi.org/10.1038/ncomms10082

Biastoch, A., Lutjeharms, J. R. E., Böning, C. W., & Scheinert, M. (2008). Mesoscale perturbations control inter-ocean exchange south of Africa. *Geophysical Research Letters*, *35*, L20602. https://doi.org/10.1029/2008GL035132

Brett, A., Leape, J., Abbott, M., Sakaguchi, H., Cao, L., Chand, K., et al. (2020). Ocean data need a sea change to help navigate the warming world. *Nature*, *582*(7811), 181–183. https://doi.org/10.1038/d41586-020-01668-z

Buongiorno Nardelli, B. (2012). A novel approach for the high-resolution interpolation of in situ sea surface salinity. *Journal of Atmospheric and Oceanic Technology*, *29*(6), 867–879. https://doi.org/10.1175/JTECH-D-11-00099.1

Buongiorno Nardelli, B., Mulet, S., & Iudicone, D. (2018). Three-dimensional ageostrophic motion and water mass subduction in the Southern Ocean. *Journal of Geophysical Research: Oceans*, *123*, 1533–1562. https://doi.org/10.1002/2017JC013316

Cancet, M., Griffin, D., Cahill, M., Chapron, B., Johannessen, J., & Donlon, C. (2019). Evaluation of GlobCurrent surface ocean current products: A case study in Australia. *Remote Sensing of Environment*, *220*, 71–93. https://doi.org/10.1016/j.rse.2018.10.029

Capet, X., Klein, P., Hua, B. L., Lapeyre, G., & McWilliams, J. C. (2008). Surface kinetic energy transfer in surface quasi-geostrophic flows. *Journal of Fluid Mechanics*, *604*, 165–174. https://doi.org/10.1017/S0022112008001110

Capuano, T. A., Speich, S., Carton, X., & Laxenaire, R. (2018). Indo-Atlantic exchange, mesoscale dynamics, and Antarctic intermediate water. *Journal of Geophysical Research: Oceans*, *123*, 3286–3306. https://doi.org/10.1002/2017JC013521

Casanova-Masjoan, M., Pelegrí, J. L., Sangrà, P., Martínez, A., Grisolía-Santos, D., Pérez-Hernández, M. D., & Hernández-Guerra, A. (2017). Characteristics and evolution of an Agulhas ring. *Journal of Geophysical Research: Oceans*, *122*, 7049–7065. https://doi.org/10.1002/2017JC012969

Chaigneau, A., Le Texier, M., Eldin, G., Grados, C., & Pizarro, O. (2011). Vertical structure of mesoscale eddies in the eastern South Pacific Ocean: A composite analysis from altimetry and Argo profiling floats. *Journal of Geophysical Research*, *116*, C11025. https://doi.org/10.1029/2011JC007134

Chavanne, C. P., & Klein, P. (2016). Quasigeostrophic diagnosis of mixed layer dynamics embedded in a mesoscale turbulent field. *Journal of Physical Oceanography*, *46*(1), 275–287. https://doi.org/10.1175/JPO-D-14-0178.1

Chelton, D. B., de Szoeke, R. A., Schlax, M. G., El Naggar, K., & Siwertz, N. (1998). Geographical variability of the first baroclinic Rossby radius of deformation. *Journal of Physical Oceanography*, *28*(3), 433–460. https://doi.org/10.1175/1520-0485(1998)028<0433:GVOTFB>2.0.CO;2

Chelton, D. B., Gaube, P., Schlax, M. G., Early, J. J., & Samelson, R. M. (2011). The influence of nonlinear mesoscale eddies on near-surface oceanic chlorophyll. *Science*, *334*(6054), 328–332. https://doi.org/10.1126/science.1208897

Chelton, D. B., Schlax, M. G., & Samelson, R. M. (2011). Global observations of nonlinear mesoscale eddies. *Progress in Oceanography*, *91*(2), 167–216. https://doi.org/10.1016/j.pocean.2011.01.002

Chen, G., Hou, Y., & Chu, X. (2011). Mesoscale eddies in the South China Sea: Mean properties, spatiotemporal variability, and impact on thermohaline structure. *Journal of Geophysical Research*, *116*, C06018. https://doi.org/10.1029/2010JC006716

Chen, Z., Wang, X., & Liu, L. (2020). Reconstruction of three-dimensional ocean structure from sea surface data: An application of isQG method in the Southwest Indian Ocean. *Journal of Geophysical Research: Oceans*, *125*, e2020JC016351. https://doi.org/10.1029/2020JC016351

Chen, Z., Wang, X., Liu, L., & Wang, X. (2023). Supporting data for estimating three-dimensional structures of eddy in the South Indian Ocean from the satellite observations based on the isQG method (1.0) [Dataset]. Zenodo. https://doi.org/10.5281/ZENODO.8140630

CLIVAR and Carbon Hydrographic Data Office. (2023). GO-SHIP subsurface velocity and T/S profiles [Dataset]. Retrieved from https://cchdo.ucsd.edu/search?q=GO-SHIP

Copernicus Marine Service. (2023a). Global ocean gridded L4 sea surface heights and derived variables reprocessed 1993 ongoing [Dataset]. https://doi.org/10.48670/moi-00148

Copernicus Marine Service. (2023b). Global ocean mean dynamic topography [Dataset]. https://doi.org/10.48670/moi-00150

Copernicus Marine Service. (2023c). Global ocean physics reanalysis [Dataset]. https://doi.org/10.48670/moi-00021

Ding, M., Liu, H., Lin, P., Hu, A., Meng, Y., Li, Y., & Liu, K. (2022). Overestimated eddy kinetic energy in the eddy-rich regions simulated by eddy-resolving global ocean–sea ice models. *Geophysical Research Letters*, *49*, e2022GL098370. https://doi.org/10.1029/2022GL098370

Dong, C., Liu, L., Nencioli, F., Bethel, B. J., Liu, Y., Xu, G., et al. (2022). The near-global ocean mesoscale eddy atmospheric–oceanic–biological interaction observational dataset. *Scientific Data*, *9*(1), 436. https://doi.org/10.1038/s41597-022-01550-9

Dong, C., McWilliams, J. C., Liu, Y., & Chen, D. (2014). Global heat and salt transports by eddy movement. *Nature Communications*, *5*(1), 3294. https://doi.org/10.1038/ncomms4294

Dong, D., Brandt, P., Chang, P., Schütte, F., Yang, X., Yan, J., & Zeng, J. (2017). Mesoscale eddies in the northwestern Pacific Ocean: Three-dimensional eddy structures and heat/salt transports. *Journal of Geophysical Research: Oceans*, *122*, 9795–9813. https://doi.org/10.1002/2017JC013303

Dufois, F., Hardman-Mountford, N. J., Fernandes, M., Wojtasiewicz, B., Shenoy, D., Slawinski, D., et al. (2017). Observational insights into chlorophyll distributions of subtropical South Indian Ocean eddies: Chlorophyll in subtropical gyre eddies. *Geophysical Research Letters*, *44*, 3255–3264. https://doi.org/10.1002/2016GL072371

Ferrari, R., & Wunsch, C. (2009). Ocean circulation kinetic energy: Reservoirs, sources, and sinks. *Annual Review of Fluid Mechanics*, *41*(1), 253–282. https://doi.org/10.1146/annurev.fluid.40.111406.102139

Fiedler, E. K., Mao, C., Good, S. A., Waters, J., & Martin, M. J. (2019). Improvements to feature resolution in the OSTIA sea surface temperature analysis using the NEMOVAR assimilation scheme. *Quarterly Journal of the Royal Meteorological Society*, *145*(725), 3609–3625. https://doi.org/10.1002/qj.3644

Gaillard, F., Reynaud, T., Thierry, V., Kolodziejczyk, N., & von Schuckmann, K. (2016). In situ–based reanalysis of the global ocean temperature and salinity with ISAS: Variability of the heat content and steric height. *Journal of Climate*, *29*(4), 1305–1323. https://doi.org/10.1175/JCLI-D-15-0028.1

Gaube, P., Chelton, D. B., Strutton, P. G., & Behrenfeld, M. J. (2013). Satellite observations of chlorophyll, phytoplankton biomass, and Ekman pumping in nonlinear mesoscale eddies. *Journal of Geophysical Research: Oceans*, *118*, 6349–6370. https://doi.org/10.1002/2013JC009027

Gentemann, C. L. (2003). Diurnal signals in satellite sea surface temperature measurements. *Geophysical Research Letters*, *30*(3), 1140. https://doi.org/10.1029/2002GL016291

González-Haro, C., & Isern-Fontanet, J. (2014). Global ocean current reconstruction from altimetric and microwave SST measurements. *Journal of Geophysical Research: Oceans*, *119*, 3378–3391. https://doi.org/10.1002/2013JC009728

González-Haro, C., Isern-Fontanet, J., Tandeo, P., & Garello, R. (2020). Ocean surface currents reconstruction: Spectral characterization of the transfer function between SST and SSH. *Journal of Geophysical Research: Oceans*, *125*, e2019JC015958. https://doi.org/10.1029/2019JC015958

He, Y., Feng, M., Xie, J., He, Q., Liu, J., Xu, J., et al. (2021). Revisit the vertical structure of the eddies and eddy-induced transport in the Leeuwin Current system. *Journal of Geophysical Research: Oceans*, *126*, e2020JC016556. https://doi.org/10.1029/2020JC016556

He, Z., Wang, X., Wu, X., Chen, Z., & Chen, J. (2021). Projecting three-dimensional ocean thermohaline structure in the North Indian Ocean from the satellite sea surface data based on a variational method. *Journal of Geophysical Research: Oceans*, *126*, e2020JC016759. https://doi.org/10.1029/2020JC016759

Hoskins, B. J. (1975). The geostrophic momentum approximation and the semi-geostrophic equations. *Journal of the Atmospheric Sciences*, *32*(2), 233–242. https://doi.org/10.1175/1520-0469(1975)032<0233:TGMAAT>2.0.CO;2

Hughes, C. W., & Wilson, C. (2008). Wind work on the geostrophic ocean circulation: An observational study of the effect of small scales in the wind stress. *Journal of Geophysical Research*, *113*, C02016. https://doi.org/10.1029/2007JC004371

IOC, SCOR, & IAPSO. (2010). The international thermodynamic equation of seawater—2010: Calculation and use of thermodynamic properties. In *Intergovernmental Oceanographic Commission, manuals and guides, 56* (pp. 196). UNESCO. Retrieved from http://www.teos-10.org/pubs/TEOS-10_Manual.pdf

Isern-Fontanet, J., Ballabrera-Poy, J., Turiel, A., & García-Ladona, E. (2017). Remote sensing of ocean surface currents: A review of what is being observed and what is being assimilated. *Nonlinear Processes in Geophysics*, *24*(4), 613–643. https://doi.org/10.5194/npg-24-613-2017

Isern-Fontanet, J., Chapron, B., Lapeyre, G., & Klein, P. (2006). Potential use of microwave sea surface temperatures for the estimation of ocean currents. *Geophysical Research Letters*, *33*, L24608. https://doi.org/10.1029/2006GL027801

Isern-Fontanet, J., Lapeyre, G., Klein, P., Chapron, B., & Hecht, M. W. (2008). Three-dimensional reconstruction of oceanic mesoscale currents from surface information. *Journal of Geophysical Research*, *113*, C09005. https://doi.org/10.1029/2007JC004692

Isern-Fontanet, J., Shinde, M., & González-Haro, C. (2014). On the transfer function between surface fields and the geostrophic stream function in the Mediterranean Sea. *Journal of Physical Oceanography*, *44*(5), 1406–1423. https://doi.org/10.1175/JPO-D-13-0186.1

Jean-Michel, L., Eric, G., Romain, B.-B., Gilles, G., Angélique, M., Marie, D., et al. (2021). The Copernicus global 1/12° oceanic and sea ice GLORYS12 reanalysis. *Frontiers in Earth Science*, *9*, 698876. https://doi.org/10.3389/feart.2021.698876

José, Y. S., Aumont, O., Machu, E., Penven, P., Moloney, C. L., & Maury, O. (2014). Influence of mesoscale eddies on biological production in the Mozambique Channel: Several contrasted examples from a coupled ocean–biogeochemistry model. *Deep Sea Research Part II: Topical Studies in Oceanography*, *100*, 79–93. https://doi.org/10.1016/j.dsr2.2013.10.018

Klein, P., Isern-Fontanet, J., Lapeyre, G., Roullet, G., Danioux, E., Chapron, B., et al. (2009). Diagnosis of vertical velocities in the upper ocean from high resolution sea surface height. *Geophysical Research Letters*, *36*, L12603. https://doi.org/10.1029/2009GL038359

Klein, P., & Lapeyre, G. (2009). The oceanic vertical pump induced by mesoscale and submesoscale turbulence. *Annual Review of Marine Science*, *1*(1), 351–375. https://doi.org/10.1146/annurev.marine.010908.163704

Kolodziejczyk, N., Prigent-Mazella, A., & Gaillard, F. (2021). *ISAS temperature and salinity gridded fields*. SEANOE. https://doi.org/10.17882/52367

LaCasce, J. H. (2012). Surface quasigeostrophic solutions and baroclinic modes with exponential stratification. *Journal of Physical Oceanography*, *42*(4), 569–580. https://doi.org/10.1175/JPO-D-11-0111.1

LaCasce, J. H., & Groeskamp, S. (2020). Baroclinic modes over rough bathymetry and the surface deformation radius. *Journal of Physical Oceanography*, *50*(10), 2835–2847. https://doi.org/10.1175/JPO-D-20-0055.1

LaCasce, J. H., & Mahadevan, A. (2006). Estimating subsurface horizontal and vertical velocities from sea-surface temperature. *Journal of Marine Research*, *64*(5), 695–721. https://doi.org/10.1357/002224006779367267

LaCasce, J. H., & Wang, J. (2015). Estimating subsurface velocities from surface fields with idealized stratification. *Journal of Physical Oceanography*, *45*(9), 2424–2435. https://doi.org/10.1175/JPO-D-14-0206.1

Lapeyre, G. (2009). What vertical mode does the altimeter reflect? On the decomposition in baroclinic modes and on a surface-trapped mode. *Journal of Physical Oceanography*, *39*(11), 2857–2874. https://doi.org/10.1175/2009JPO3968.1

Lapeyre, G. (2017). Surface quasi-geostrophy. *Fluids*, *2*(1), 7. https://doi.org/10.3390/fluids2010007

Lapeyre, G., & Klein, P. (2006). Dynamics of the upper oceanic layers in terms of surface quasigeostrophy theory. *Journal of Physical Oceanography*, *36*(2), 165–176. https://doi.org/10.1175/JPO2840.1

Laurindo, L. C., Mariano, A. J., & Lumpkin, R. (2017). An improved near-surface velocity climatology for the global ocean from drifter observations. *Deep Sea Research Part I: Oceanographic Research Papers*, *124*, 73–92. https://doi.org/10.1016/j.dsr.2017.04.009

Liu, L., Peng, S., & Huang, R. X. (2017). Reconstruction of ocean's interior from observed sea surface information: Ocean's interior reconstruction. *Journal of Geophysical Research: Oceans*, *122*, 1042–1056. https://doi.org/10.1002/2016JC011927

Liu, L., Peng, S., Wang, J., & Huang, R. X. (2014). Retrieving density and velocity fields of the ocean's interior from surface data. *Journal of Geophysical Research: Oceans*, *119*, 8512–8529. https://doi.org/10.1002/2014JC010221

Liu, L., & Xue, H. (2022). Estimating the ocean interior from satellite observations in the Kerguelen area (Southern Ocean): A combined investigation using high-resolution CTD data from animal-borne instruments. *Journal of Physical Oceanography*, *52*(10), 2463–2478. https://doi.org/10.1175/JPO-D-21-0183.1

Liu, L., Xue, H., & Sasaki, H. (2019). Reconstructing the ocean interior from high-resolution sea surface information. *Journal of Physical Oceanography*, *49*(12), 3245–3262. https://doi.org/10.1175/JPO-D-19-0118.1

Liu, L., Xue, H., & Sasaki, H. (2021). Diagnosing subsurface vertical velocities from high-resolution sea surface fields. *Journal of Physical Oceanography*, *51*(5), 1353–1373. https://doi.org/10.1175/JPO-D-20-0152.1

Liu, Y., & Weisberg, R. H. (2011). Evaluation of trajectory modeling in different dynamic regions using normalized cumulative Lagrangian separation. *Journal of Geophysical Research*, *116*, C09013. https://doi.org/10.1029/2010JC006837

Liu, Y., Weisberg, R. H., Vignudelli, S., & Mitchum, G. T. (2014). Evaluation of altimetry-derived surface current products using Lagrangian drifter trajectories in the eastern Gulf of Mexico. *Journal of Geophysical Research: Oceans*, *119*, 2827–2842. https://doi.org/10.1002/2013JC009710

Lumpkin, R., Grodsky, S. A., Centurioni, L., Rio, M.-H., Carton, J. A., & Lee, D. (2013). Removing spurious low-frequency variability in drifter velocities. *Journal of Atmospheric and Oceanic Technology*, *30*(2), 353–360. https://doi.org/10.1175/JTECH-D-12-00139.1

Martin, M., Dash, P., Ignatov, A., Banzon, V., Beggs, H., Brasnett, B., et al. (2012). Group for high resolution sea surface temperature (GHRSST) analysis fields inter-comparisons. Part 1: A GHRSST multi-product ensemble (GMPE). *Deep Sea Research Part II: Topical Studies in Oceanography*, *77–80*, 21–30. https://doi.org/10.1016/j.dsr2.2012.04.013

Martin, S. A., Manucharyan, G. E., & Klein, P. (2023). Synthesizing sea surface temperature and satellite altimetry observations using deep learning improves the accuracy and resolution of gridded sea surface height anomalies. *Journal of Advances in Modeling Earth Systems*, *15*, e2022MS003589. https://doi.org/10.1029/2022MS003589

McGillicuddy, D. J., Anderson, L. A., Bates, N. R., Bibby, T., Buesseler, K. O., Carlson, C. A., et al. (2007). Eddy/wind interactions stimulate extraordinary mid-ocean plankton blooms. *Science*, *316*(5827), 1021–1026. https://doi.org/10.1126/science.1136256

Miracca-Lage, M., González-Haro, C., Napolitano, D. C., Isern-Fontanet, J., & Polito, P. S. (2022). Can the surface quasi-geostrophic (SQG) theory explain upper ocean dynamics in the South Atlantic? *Journal of Geophysical Research: Oceans*, *127*, e2021JC018001. https://doi.org/10.1029/2021JC018001

Morrow, R., Fu, L.-L., Ardhuin, F., Benkiran, M., Chapron, B., Cosme, E., et al. (2019). Global observations of fine-scale ocean surface topography with the surface water and ocean topography (SWOT) mission. *Frontiers in Marine Science*, *6*, 232. https://doi.org/10.3389/fmars.2019.00232

Mulet, S., Rio, M.-H., Etienne, H., Artana, C., Cancet, M., Dibarboure, G., et al. (2021). The new CNES-CLS18 global mean dynamic topography. *Ocean Science*, *17*(3), 789–808. https://doi.org/10.5194/os-17-789-2021

National Centers for Environmental Information. (2023). WOA 2018 data access: Statistical mean of temperature on 1° grid for all decades [Dataset]. Retrieved from https://www.nodc.noaa.gov/cgi-bin/OC5/woa18/woa18.pl

National Oceanic and Atmospheric Administration Atlantic Oceanographic and Meteorological Laboratory. (2023). NOAA Global Drifter Program quality-controlled 6-hour interpolated data from ocean surface drifting buoys [Dataset]. https://doi.org/10.25921/7ntx-z961

Nencioli, F., Dall'Olmo, G., & Quartly, G. D. (2018). Agulhas ring transport efficiency from combined satellite altimetry and Argo profiles. *Journal of Geophysical Research: Oceans*, *123*, 5874–5888. https://doi.org/10.1029/2018JC013909

Olmedo, E., González-Haro, C., Hoareau, N., Umbert, M., González-Gambau, V., Martínez, J., et al. (2021). Nine years of SMOS sea surface salinity global maps at the Barcelona Expert Center. *Earth System Science Data*, *13*(2), 857–888. https://doi.org/10.5194/essd-13-857-2021

Olmedo, E., Martínez, J., Turiel, A., Ballabrera-Poy, J., & Portabella, M. (2017). Debiased non-Bayesian retrieval: A novel approach to SMOS sea surface salinity. *Remote Sensing of Environment*, *193*, 103–126. https://doi.org/10.1016/j.rse.2017.02.023

Pedlosky, J. (1987). *Geophysical fluid dynamics*. Springer-Verlag. https://doi.org/10.1007/978-1-4684-0071-7

Pegliasco, C., Chaigneau, A., & Morrow, R. (2015). Main eddy vertical structures observed in the four major Eastern Boundary Upwelling Systems. *Journal of Geophysical Research: Oceans*, *120*, 6008–6033. https://doi.org/10.1002/2015JC010950

Ponte, A. L., & Klein, P. (2013). Reconstruction of the upper ocean 3D dynamics from high-resolution sea surface height. *Ocean Dynamics*, *63*(7), 777–791. https://doi.org/10.1007/s10236-013-0611-7

Ponte, A. L., Klein, P., Capet, X., Le Traon, P.-Y., Chapron, B., & Lherminier, P. (2013). Diagnosing surface mixed layer dynamics from high-resolution satellite observations: Numerical insights. *Journal of Physical Oceanography*, *43*(7), 1345–1355. https://doi.org/10.1175/JPO-D-12-0136.1

Pujol, M.-I., Dibarboure, G., Le Traon, P.-Y., & Klein, P. (2012). Using high-resolution altimetry to observe mesoscale signals. *Journal of Atmospheric and Oceanic Technology*, *29*(9), 1409–1416. https://doi.org/10.1175/JTECH-D-12-00032.1

Qiu, B., & Chen, S. (2005). Eddy-induced heat transport in the subtropical North Pacific from Argo, TMI, and altimetry measurements. *Journal of Physical Oceanography*, *35*(4), 458–473. https://doi.org/10.1175/JPO2696.1

Qiu, B., Chen, S., Klein, P., Torres, H., Wang, J., Fu, L.-L., & Menemenlis, D. (2020). Reconstructing upper-ocean vertical velocity field from sea surface height in the presence of unbalanced motion. *Journal of Physical Oceanography*, *50*(1), 55–79. https://doi.org/10.1175/JPO-D-19-0172.1

Qiu, B., Chen, S., Klein, P., Ubelmann, C., Fu, L.-L., & Sasaki, H. (2016). Reconstructability of three-dimensional upper-ocean circulation from SWOT sea surface height measurements. *Journal of Physical Oceanography*, *46*(3), 947–963. https://doi.org/10.1175/JPO-D-15-0188.1

Remote Sensing Systems. (2023). Microwave and infrared OI SST product description [Dataset]. Retrieved from https://data.remss.com/SST/daily/mw_ir/v05.1/

Reynolds, R. W., & Chelton, D. B. (2010). Comparisons of daily sea surface temperature analyses for 2007–08. *Journal of Climate*, *23*(13), 3545–3562. https://doi.org/10.1175/2010JCLI3294.1

Reynolds, R. W., Chelton, D. B., Roberts-Jones, J., Martin, M. J., Menemenlis, D., & Merchant, C. J. (2013). Objective determination of feature resolution in two sea surface temperature analyses. *Journal of Climate*, *26*(8), 2514–2533. https://doi.org/10.1175/JCLI-D-12-00787.1

Rio, M.-H., & Santoleri, R. (2018). Improved global surface currents from the merging of altimetry and sea surface temperature data. *Remote Sensing of Environment*, *216*, 770–785. https://doi.org/10.1016/j.rse.2018.06.003

Riser, S. C., Freeland, H. J., Roemmich, D., Wijffels, S., Troisi, A., Belbéoch, M., et al. (2016). Fifteen years of ocean observations with the global Argo array. *Nature Climate Change*, *6*(2), 145–153. https://doi.org/10.1038/nclimate2872

Sasaki, H., & Klein, P. (2012). SSH wavenumber spectra in the North Pacific from a high-resolution realistic simulation. *Journal of Physical Oceanography*, *42*(7), 1233–1241. https://doi.org/10.1175/JPO-D-11-0180.1

SEANOE. (2021). ISAS temperature and salinity gridded fields [Dataset]. https://doi.org/10.17882/52367

Sen, A., Scott, R. B., & Arbic, B. K. (2008). Global energy dissipation rate of deep-ocean low-frequency flows by quadratic bottom boundary layer drag: Computations from current-meter data. *Geophysical Research Letters*, *35*, L09606. https://doi.org/10.1029/2008GL033407

Sheen, K. L., Naveira Garabato, A. C., Brearley, J. A., Meredith, M. P., Polzin, K. L., Smeed, D. A., et al. (2014). Eddy-induced variability in Southern Ocean abyssal mixing on climatic timescales. *Nature Geoscience*, *7*(8), 577–582. https://doi.org/10.1038/ngeo2200

Souza, J. M. A. C., de Boyer Montégut, C., Cabanes, C., & Klein, P. (2011). Estimation of the Agulhas ring impacts on meridional heat fluxes and transport using ARGO floats and satellite data. *Geophysical Research Letters*, *38*, L21602. https://doi.org/10.1029/2011GL049359

Stammer, D. (1998). On eddy characteristics, eddy transports, and mean flow properties. *Journal of Physical Oceanography*, *28*(4), 727–739. https://doi.org/10.1175/1520-0485(1998)028<0727:OECETA>2.0.CO;2

Taburet, G., Sanchez-Roman, A., Ballarotta, M., Pujol, M.-I., Legeais, J.-F., Fournier, F., et al. (2019). DUACS DT2018: 25 years of reprocessed sea level altimetry products. *Ocean Science*, *15*(5), 1207–1224. https://doi.org/10.5194/os-15-1207-2019

Talley, L. D., Pickard, G. L., Emery, W. J., & Swift, J. H. (2011). *Descriptive physical oceanography: An introduction* (6th ed.). Academic Press. https://doi.org/10.1016/C2009-0-24322-4

The MathWorks Inc. (2022). MATLAB version: 9.13.0 (R2022b) [Software]. The MathWorks Inc. Retrieved from https://www.mathworks.com/

Torres, H. S., Klein, P., D'Asaro, E., Wang, J., Thompson, A. F., Siegelman, L., et al. (2022). Separating energetic internal gravity waves and small-scale frontal dynamics. *Geophysical Research Letters*, *49*, e2021GL096249. https://doi.org/10.1029/2021GL096249

Tulloch, R., & Smith, K. S. (2006). A new theory for the atmospheric energy spectrum: Depth-limited temperature anomalies at the tropopause. *Proceedings of the National Academy of Sciences of the United States of America*, *103*(40), 14690–14694. https://doi.org/10.1073/pnas.0605494103

Ubelmann, C., Carrere, L., Durand, C., Dibarboure, G., Faugère, Y., Ballarotta, M., et al. (2022). Simultaneous estimation of ocean mesoscale and coherent internal tide sea surface height signatures from the global altimetry record. *Ocean Science*, *18*(2), 469–481. https://doi.org/10.5194/os-18-469-2022

Ubelmann, C., Dibarboure, G., Gaultier, L., Ponte, A., Ardhuin, F., Ballarotta, M., & Faugère, Y. (2021). Reconstructing ocean surface current combining altimetry and future spaceborne Doppler data. *Journal of Geophysical Research: Oceans*, *126*, e2020JC016560. https://doi.org/10.1029/2020JC016560

Wang, J., Flierl, G. R., LaCasce, J. H., McClean, J. L., & Mahadevan, A. (2013). Reconstructing the ocean's interior from surface data. *Journal of Physical Oceanography*, *43*(8), 1611–1626. https://doi.org/10.1175/JPO-D-12-0204.1

Wang, X., Li, W., Qi, Y., & Han, G. (2012). Heat, salt and volume transports by eddies in the vicinity of the Luzon Strait. *Deep Sea Research Part I: Oceanographic Research Papers*, *61*, 21–33. https://doi.org/10.1016/j.dsr.2011.11.006

Yan, H., Wang, H., Zhang, R., Chen, J., Bao, S., & Wang, G. (2020). A dynamical–statistical approach to retrieve the ocean interior structure from surface data: SQG-mEOF-R. *Journal of Geophysical Research: Oceans*, *125*, e2019JC015840. https://doi.org/10.1029/2019JC015840

Yan, H., Zhang, R., Wang, H., Bao, S., Chen, J., & Wang, G. (2021). A surface quasi-geostrophic-based dynamical–statistical framework to retrieve interior temperature/salinity from ocean surface. *Journal of Geophysical Research: Oceans*, *126*, e2020JC017139. https://doi.org/10.1029/2020JC017139

Yang, G., Wang, F., Li, Y., & Lin, P. (2013). Mesoscale eddies in the northwestern subtropical Pacific Ocean: Statistical characteristics and three-dimensional structures: Eddies in the Northwestern Pacific. *Journal of Geophysical Research: Oceans*, *118*, 1906–1925. https://doi.org/10.1002/jgrc.20164

Yang, Y., Wang, D., Wang, Q., Zeng, L., Xing, T., He, Y., et al. (2019). Eddy-induced transport of saline Kuroshio water into the northern South China Sea. *Journal of Geophysical Research: Oceans*, *124*, 6673–6687. https://doi.org/10.1029/2018JC014847

Zhai, X., Johnson, H. L., & Marshall, D. P. (2010). Significant sink of ocean-eddy energy near western boundaries. *Nature Geoscience*, *3*(9), 608–612. https://doi.org/10.1038/ngeo943

Zhang, Y., Liu, Z., Zhao, Y., Wang, W., Li, J., & Xu, J. (2014). Mesoscale eddies transport deep-sea sediments. *Scientific Reports*, *4*(1), 5937. https://doi.org/10.1038/srep05937

Zhang, Z., Tian, J., Qiu, B., Zhao, W., Chang, P., Wu, D., & Wan, X. (2016). Observed 3D structure, generation, and dissipation of oceanic mesoscale eddies in the South China Sea. *Scientific Reports*, *6*(1), 24349. https://doi.org/10.1038/srep24349

Zhang, Z., Wang, W., & Qiu, B. (2014). Oceanic mass transport by mesoscale eddies. *Science*, *345*(6194), 322–324. https://doi.org/10.1126/science.1252418

Zhang, Z., Zhang, Y., Wang, W., & Huang, R. X. (2013). Universal structure of mesoscale eddies in the ocean: Structure of oceanic geostrophic eddies. *Geophysical Research Letters*, *40*, 3677–3681. https://doi.org/10.1002/grl.50736

Zhang, Z., Zhao, W., Tian, J., & Liang, X. (2013). A mesoscale eddy pair southwest of Taiwan and its influence on deep circulation: Mesoscale eddy southwest of Taiwan. *Journal of Geophysical Research: Oceans*, *118*, 6479–6494. https://doi.org/10.1002/2013JC008994

Zheng, S., Du, Y., Li, J., & Cheng, X. (2015). Eddy characteristics in the South Indian Ocean as inferred from surface drifters. *Ocean Science*, *11*(3), 361–371. https://doi.org/10.5194/os-11-361-2015

Zhou, G., & Cheng, X. (2021). On the errors of estimating oceanic eddy kinetic energy. *Journal of Geophysical Research: Oceans*, *126*(2), e2020JC016449. https://doi.org/10.1029/2020jc016449